Role of dopant in the formation of reactive oxygen species and oxidation catalysis on CeO₂(111)

Md. Saeedur Rahman and Ye Xu*

Cain Department of Chemical Engineering, Louisiana State University, Baton Rouge, Louisiana 70803, United States

^{*} Corresponding author. Email address: yexu@lsu.edu (Y. Xu).

Abstract

We theoretically investigate the role of nine 3d-5d Groups 9-11 metals substitutionally doped into CeO₂(111) in terms of *i*) oxygen vacancy (V_O) formation; *ii*) H and CO adsorption; *iii*) H₂ oxidation, C₃H₈ oxidative dehydrogenation, and CO oxidation. Lattice O and O₂ species at the doped sites are significantly more active toward binding H and CO than in un-doped CeO₂(111). All the dopants lower the V_O formation energy vs. un-doped CeO₂(111), which becomes negative for Ni, Pd, Pt, Cu, and Ag. The square planar structure is energetically preferred by all the doped V_O. Whether doping promotes the catalysis of the oxidation reactions depends on which of the chemisorption, V_O formation, and surface re-oxidation steps is the bottleneck. When the V_O formation step is, doping is expected to have little promotional effect, because V_O formation is an *iso-reduction* step whose reaction energy is independent of doping.

1 Introduction

Ceria is a prototypical reducible oxide that is fairly abundant in Earth's crust. As a catalyst carrier or promoter, it enhances metal-catalyzed redox reactions including water-gas shift, hydrocarbon reforming, and automotive three-way catalysis. It also catalyzes total oxidation or combustion of CO, NO, soot, hydrocarbons, and volatile organic compounds (VOCs) at elevated temperatures (ranging from 150 °C for chlorinated hydrocarbons to 400 °C for soot) [1]. Recently, ceria nanoparticles have come to be recognized for their bio-catalytic activity by mimicking the action of enzymes including peroxidase, superoxide dismutase, oxidase, and phosphatase at physiological conditions [2]. This raises an interesting question whether ceria can be modified to catalyze gasphase oxidation reactions at ambient temperature. Catalytic materials capable of destroying harmful compounds are of practical utility in environmental protection and remediation technologies. Permanganate-based products for removing VOCs from air are available commercially, but they have limited lifetime, and function more as reactive sorbents than catalysts.

Doping ceria has been widely practiced in the heterogeneous catalysis community for the purpose of enhancing the catalytic or other technologically relevant properties of ceria. However, a quantifiable mechanistic rationale for doing so is often lacking. The literature on catalysis by doped ceria (not considering metals supported thereon) shows that mid-to-late transition metal (TM) dopants including Fe, Mn, Ni, Cu, Rh, Pd, and Pt boost the catalytic activity of ceria for reactions including CO oxidation [3-9], soot combustion [4, 10, 11], hydrocarbon combustion [3, 12, 13], VOC combustion [12, 14], and water-gas shift [15, 16], while early TM and rare earth (RE) elements such as Zr, Y, La, and Gd do not appear to have any notable effects [3, 4, 12]. For CO oxidation, dopants including Fe, Mn, Cu, Rh, and Pd have been shown to lower the light-off temperature by 100~200 °C [3, 4, 9] although no dopant has yet to achieve 50% conversion at

ambient temperature. A caveat is warranted: While early TM and RE elements can form solid solutions with ceria, mid-to-late TM elements do not have high solubility in ceria. Over the years, different synthesis methods have been devised to introduce TM atoms into ceria, including coprecipitation [3, 11] and co-combustion [17]. Still, the location of dopant atoms cannot be precisely controlled and identified. They may be deep inside the oxide lattice, near the surface, or on the surface. They may be atomically dispersed or aggregate into a separate phase of metal or metal oxide clusters. Consequently, catalytic measurements of doped ceria cannot always be unambiguously interpreted. This is where theory can help by shedding light on the effects of dopants in different phases on ceria.

Krcha et al. systematically modeled substitutional doping of $CeO_2(111)$ by nearly all 3d, 4d, and 5d TM atoms calculated using GGA-PW91 with U=5 eV [18]. *Substitutional* doping refers to the replacement of a Ce atom at its lattice position with an atom of another metal. Nearly all the TM elements are found to enhance the reducibility of ceria, i.e., making the formation energy of an oxygen vacancy (ΔE_V) less endothermic when substitutionally doped into ceria, with later TMs having larger effects. The authors furthermore showed that a more exothermic ΔE_V correlates with a lower activation barrier for breaking the initial C-H bond in methane at a doped site. Other DFT studies considered some subsets of TM as dopants in CeO_2 surfaces for other reactions [19-24]. No study has compared the same dopants for different oxidation reactions on ceria.

This work attempts to lay out a theoretical framework in which to estimate the effects of dopant metals on a given oxidation reaction based on theoretically computed energetic parameters, and to predict whether a dopant can promote an oxidation reaction. We use nine Group 9-11 3d, 4d, and 5d metal elements (Co, Rh, Ir, Ni, Pd, Pt, Cu, Ag, and Au) substitutionally doped into CeO₂(111) as examples. We begin by examining how the dopants affect the local lattice in terms

of oxygen vacancy formation. Both oxygen atoms and molecular O₂ that occupy lattice oxygen sites are recognized as reactive oxygen species (ROS). The reactivity of these ROS toward H and CO, two common reductant species, is calculated and the results are used to analyze the catalytic cycles for the oxidation of H₂, a hydrocarbon – propane (C₃H₈), and CO. We show that both the removal of H as water and the removal of CO as CO₂ involve chemically and structurally similar reactant and product states, and are therefore insensitive to doping. Doping would have promotional effects on an oxidation reaction when the adsorption of the reductant species represents the energetic bottleneck in the reaction, but would not if the formation of the oxidation products via lattice oxygen extraction is the bottleneck instead.

2 Methods

Periodic spin-polarized DFT calculations were performed in the generalized gradient approximation (GGA) using the PW91 exchange-correlation functional [25] as implemented in Vienna Ab initio Simulation Package (VASP, version 5.4.4) [26]. The Projector Augmented Wave (PAW) method [27] was used to represent the potentials of the nuclei and core electrons of the elements involved, including Co/Ni/Cu(3d4s), Rh/Pd/Ag(4d5s), Ir/Pt/Au(5d6s), Ce(4f5d6s), O(2s2p), C(2s2p), and H(1s). The Kohn-Sham valence states were expanded in a plane wave basis set up to 400 eV kinetic energy cutoff. The singlet-triplet or doublet-quadruplet splitting was checked, and the lower-energy spin state for each optimized structure was used in the analysis below.

The DFT+U method developed by Dudarev et al. [28] was used to partially offset the tendency of LSDA (local spin density approximation) and GGA to delocalize strongly correlated electrons. The inherent self-interaction error prevents the localization of the 4*f* electrons on Ce

atoms that are released upon oxygen vacancy formation [29]. A small effective U value ($\lesssim 3 \text{ eV}$) has been found by multiple authors, supported by experimental measurements, to give more accurate energetics for chemical reactions [30-35], whereas a larger U value (≥ 4.5 eV) was needed to sufficiently counteract the delocalization error [31, 36, 37]. In this work, we report results obtained with U=2 eV applied to the 4f states of Ce, excepted where noted. DFT+U has also been applied to the d states in attempts to correct the self-interaction error in the description of bulk TM oxides [38]. However, it is not clear if and what U correction should be applied to the d states of TM atoms doped into ceria [39], as no systematic experimental measurements of any dopantrelated adsorption or reaction energetic parameter can be found in the literature. In this study, therefore, we chose not to apply any U value to the dopant atoms. As such, the oxidation states of the dopant atoms reported herein should be taken as the upper limit because more localized d electrons would mean a more reduced dopant atom. The calculated equilibrium lattice constant is 5.476 Å (U=2 eV) or 5.494 Å (U=5 eV), which overpredicts the experimental value of 5.41 Å [40] by less than 2%. Bader charge analysis was performed using the code of Henkelman and coworkers [41, 42] at U=5 eV due to the better description of electronic structure that a higher U value affords.

The surface model for $CeO_2(111)$ was a slab consisting of three O-Ce-O tri-layers (i.e., 9 atomic layers) with a (3×3) surface unit cell. The periodic slabs were separated by ca. 12 Å of vacuum in the z direction. The effect of a transition metal atom substitutionally doped into bulk CeO_2 or a $CeO_2(111)$ surface was modeled by replacing one Ce atom with a metal atom from Groups 9-11, including Co, Rh, Ir, Ni, Pd, Pt, Cu, Ag, and Au. Dopant atoms and adsorbates were located on one side of the slab only, with dipole corrections applied in the z direction [43]. The reciprocal space was sampled at the Γ point only. Increasing sampling to a (2×2×1) Monkhorst-

Pack k-point grid affected the electronic energy by 0.05 eV or less, so higher k-point sampling density was not used. The top two O-Ce-O tri-layers (i.e., six atomic layers) and any adsorbate thereon were relaxed when minimizing the total energy of the system, while the bottommost tri-layer was fixed at its bulk position. In modeling a dopant atom in bulk CeO₂, a $4\times4\times4$ bulk supercell was used and a V_O was introduced at a site near-neighbor (NN) to the dopant atom.

The formation energy for a point oxygen vacancy ($\Delta E_{\rm V}$) was calculated as $\Delta E_{\rm V} = E_{\rm V} + \frac{1}{2}E_{\rm O_2} - E_{\rm slab}$, and the adsorption energy ($\Delta E_{\rm A}$) was calculated as $\Delta E_{\rm A} = E_{\rm total} - E_{\rm slab}$ (or $E_{\rm V}$) – $E_{\rm A}$. Here $E_{\rm V}$ is the energy of a clean CeO₂(111) slab with an oxygen vacancy, $E_{\rm slab}$ is the energy of a clean stoichiometric CeO₂(111) slab, $E_{\rm total}$ is the energy of a CeO₂(111) slab together with an adsorbate A, and $E_{\rm O_2}$ or $E_{\rm A}$ is the energy of O₂ or another adsorbate A in the gas phase. A more negative $\Delta E_{\rm V}$ and $\Delta E_{\rm A}$ corresponds to higher reducibility and stronger adsorption, respectively. In some cases a differential adsorption energy was reported, calculated as $\delta E_{\rm A} = E_{\rm total} \,_{\rm A} - E_{\rm total} \,_{\rm A-1} - E_{\rm A}$, where $E_{\rm total} \,_{\rm A}$ and $E_{\rm total} \,_{\rm A-1}$ represent the energies of a given surface with n and n-1 molecules or atoms of A adsorbed on it, respectively. When n = 1, $\Delta E_{\rm A} = \delta E_{\rm A}$. Geometric optimization was converged to 0.03 eV/Å or less in all degrees of freedom for relaxed atoms.

Harmonic vibrational frequencies and normal modes were calculated by diagonalizing the mass-weighted Hessian matrix, i.e., second derivatives with respect to the relaxed degrees of freedom, which were approximated using a finite difference approximation with a displacement of ± 0.01 Å. Vibrational contributions to internal and free energies are not included because they are expected to be small and of similar sizes for the dopants.

3 Results and discussion

3.1 Effect of doping on structure of stoichiometric CeO₂(111)

To study the effect of doping on V_O formation in CeO₂(111), we first consider how it modifies the structure of the stoichiometric surface. In un-doped ceria, each Ce cation is coordinated to eight O_{latt} atoms at the center of a cubic arrangement, except for Ce nearest to the exposed (111) surface, which has one missing O_{latt} and therefore a maximum coordination number (CN) of 7. The dopant atoms can distort the local crystalline structure in different ways, including (the terminology does not imply perfect geometry; same below):

- Octahedral in which the dopant atom is coordinated to the three NN O atoms in the surface (1st atomic) layer and three NN O atoms in the 3rd atomic layer (Figure 1a).
- Tetrahedral in which the dopant atom is coordinated to the three NN O atoms in the 1st atomic layer and the O atom directly beneath it in the 4th atomic layer (Figure 1b). For Ag and Au, it involves the coordination of the dopant atom to the three NN O atoms in the 1st atomic layer but one NN O atom in the 3rd atomic layer instead (not shown).
- Trigonal pyramidal in which the dopant atom is coordinated to the three NN O atoms in the 3rd atomic layer and the O atom directly below it in 4th atomic layer (Figure 1c), but not to any O atom in the 1st atomic layer. The dopant atom is situated noticeably lower than the adjacent Ce atoms.
- Square planar in which the dopant atom is coordinated to one NN O atom in the 1st atomic layer, two NN O atoms in the 3rd atomic layer, and the O atom directly beneath it in 4th atomic layer (Figure 1d).
- Trigonal planar in which the dopant atom is coordinated to two NN O atoms in the 1st atomic layer and one NN O atom in the 3rd atomic layer (Figure 1e).

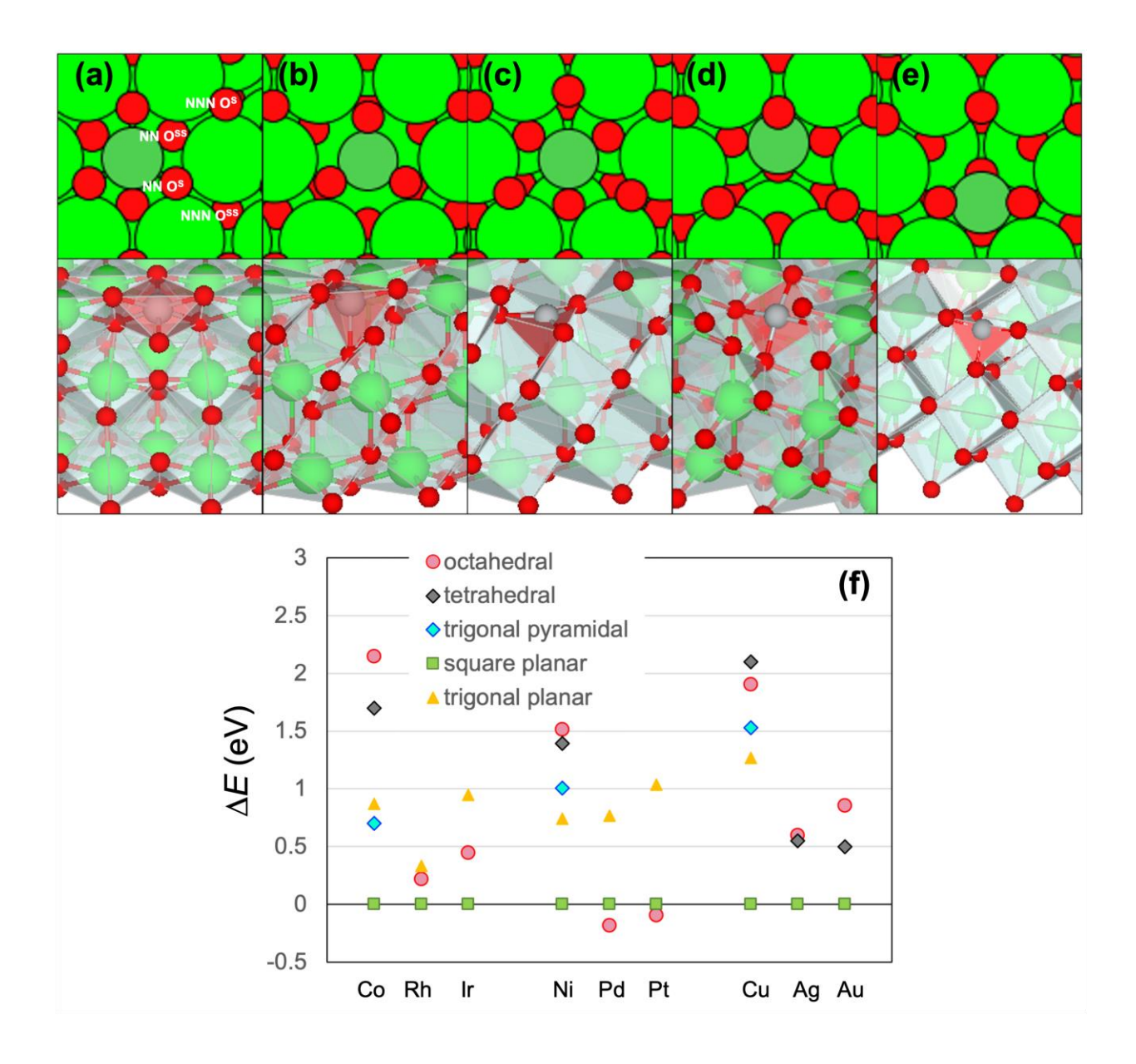


Figure 1. Different local structures for stoichiometric $CeO_2(111)$ with a Ce atom nearest to the surface (i.e., in the 2^{nd} atomic layer) substitutionally replaced by a Groups 9-11 TM atom: (a) octahedral (CN=6); (b) tetrahedral (CN=4); (c) trigonal pyramidal (CN=4); (d) square planar (CN=4); (e) trigonal planar (CN=3). Top panels show top views, and bottom panels show the same slabs tilted by various angles to show the coordination polyhedra of the dopant atom. Different lattice oxygen locations relative to dopant atom are labeled in (a), including nearest-neighbor (NN) and next-nearest-neighbor (NNN) surface (S) and sub-surface (SS) O atoms. Color code: Ce = green, O = red, dopant = other color; for clarity, the cations are shown as larger spheres than the oxygen; same below. (f) Energies of different local structures relative to that of the square

planar structure for each dopant metal. Snapshots of the minimum-energy doped structure for each dopant are shown in Figure S1 in Supporting Information (SI).

The energetics of the different coordination structures are plotted in Figure 1f. A missing structure for a dopant metal indicates that it is unstable and relaxes into one of the other structures. All except Pd and Pt prefer the square planar structure (Figure 1d) energetically. In the square planar structure, the metal-O distances are 2.0~2.1 Å for Ag and Au and less than 2 Å for Co, Rh, Ir, Ni, and Cu. Pd and Pt prefer an octahedral structure instead (Figure 1a), which appears similar to an un-doped surface except for Pd and Pt, which are more than 2.8 Å away from the O atom underneath them in the 4th atomic layer and are therefore each coordinated to only six O atoms with metal-oxygen distances of 2.1~2.2 Å. In comparison, the calculated nearest Ce-O distance in bulk CeO₂ is 2.37 Å. Increasing U from 2 eV to 5 eV does not change which structure is the most stable and which is the 2nd most stable, with the differences between the most and 2nd most stable vary by 0.2 eV or less with U (Table S1 in SI). Previously, Krcha et al. reported various dopant structures in metal-doped stoichiometric CeO₂(111) slabs [18]. The minimum-energy structure was reported to be square planar for Ag and Au; octahedral for Rh, Ir, Pd and Pt; and trigonal pyramidal for Ni and Cu. The discrepancy (which there is for Rh, Ir, Cu, and Ni) may be due in part to the smaller (2×2) surface unit cell used by Krcha et al., which restricts the extent that the lattice atoms can relax both laterally and vertically.

3.2 Effect of doping on oxygen vacancy formation in $CeO_2(111)$

The formation of V_0 in the $CeO_2(111)$ surface is studied by removing a lattice O atom at different locations with respect to the dopant atom, including the nearest-neighbor (NN) and next-nearest-

neighbor (NNN) O_{latt} sites, in either the surface or the sub-surface layer (Figure 1a). In the (3×3) unit cells used in this study, there are three equivalent NN O_{latt} sites and three equivalent NNN O_{latt} sites in the surface or the sub-surface layer relative to a dopant atom.

Below we focus on surface $V_O\left(V_O{}^S\right)$ formation at an NN site with respect to the dopant atom. Several different local coordination structures are found to be possible and are examined for all the dopant metals. They include:

- Rectangular pyramidal in which the dopant atom is coordinated to two NN O atoms in the surface layer (1st atomic layer), two NN O atoms in the 3rd atomic layer, and the O atom directly beneath it in the 4th atomic layer (Figure 2a).
- Rectangular planar this structure may be viewed as the rectangular pyramidal structure above having lost the coordination with the O atom in the 4th atomic layer (Figure 2b).
- Trigonal pyramidal this may be viewed as the structure in Figure 1c with one missing
 NN O atom in the surface layer (Figure 2c).
- Square planar this may be viewed as the structure in Figure 1d with one missing NN O atom in the surface layer (Figure 2d).
- Trigonal planar this may be viewed as the structure in Figure 1e with one missing NN O atom in the surface layer (Figure 2e).

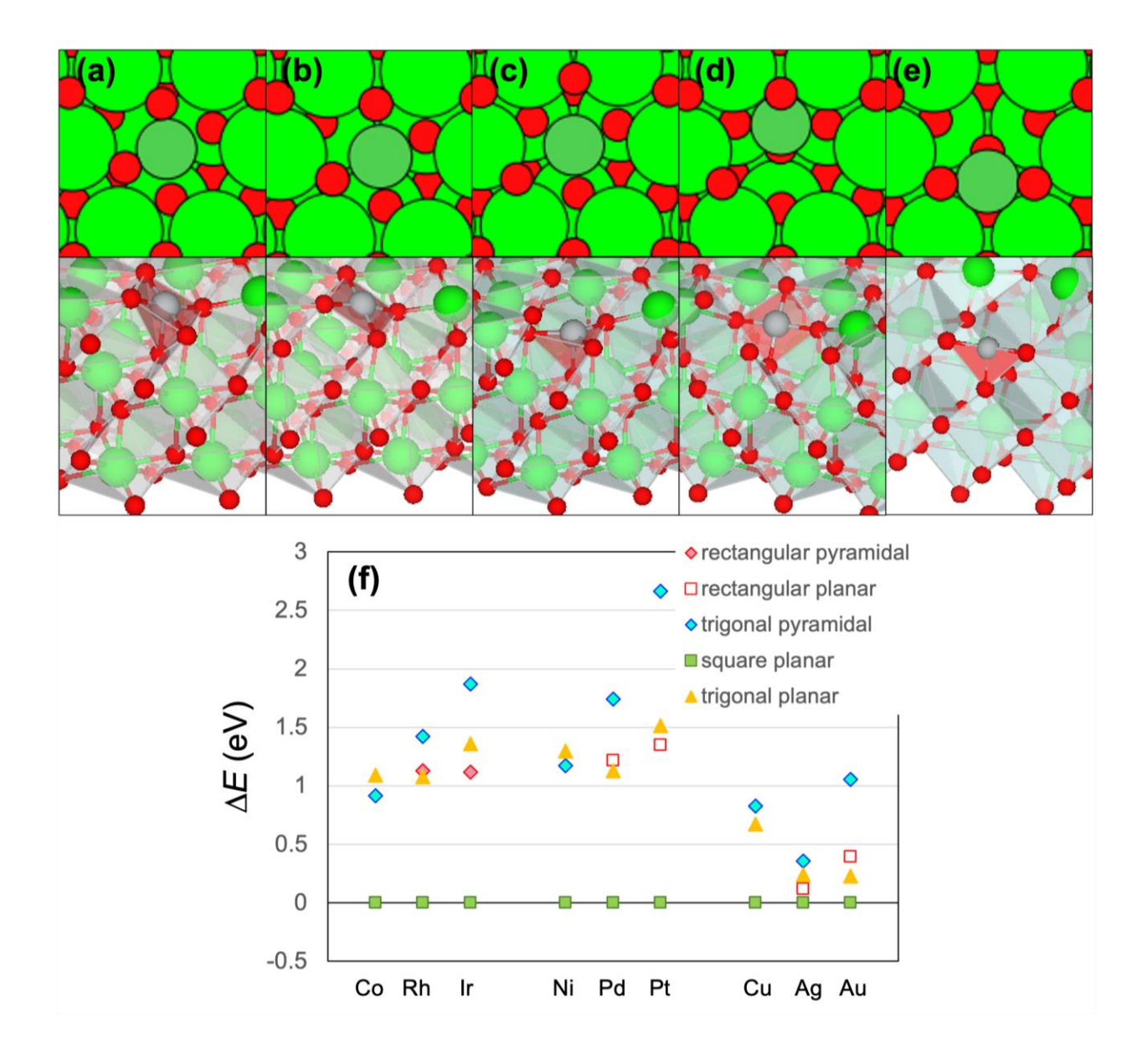


Figure 2. Different local structures for a V_O^S in $CeO_2(111)$ that is nearest-neighbor to a Ce atom in the 2^{nd} atomic layer substituted with a Groups 9-11 metal atom: (a) rectangular pyramidal (CN=5); (b) rectangular planar (CN=4); (c) trigonal pyramidal (CN=4); (d) square planar (CN=4); (e) trigonal planar (CN=3). Top panels show top views, and bottom panels show the same slabs tilted by various angles to show the coordination polyhedra of the dopant atom. (f) Energies of different local structures relative to that of the square planar structure for each dopant metal. Snapshots of the minimum-energy doped V_O^S structure for each dopant metal are shown in Figure S2.

As shown in Figure 2f, the minimum-energy NN V_O^S is a square planar structure (CN=4) with all nine dopant metals considered here. ΔE_V is substantially less positive with all nine dopant metals than for un-doped $CeO_2(111)$, i.e., substitutional doping with these metals enhances the reducibility of $CeO_2(111)$, and the much smaller $|\Delta E_V|$ values suggest more reversible vacancy formation upon doping. In each group of metals, the 4d element makes $CeO_2(111)$ more reducible than the 3d and 5d elements. Of these, Ni, Pd, Pt, Cu, and Ag yield negative, or exothermic, ΔE_V for V_O^S , suggesting spontaneous formation V_O . One would expect to find higher concentrations of V_O in $CeO_2(111)$ doped with these metals than un-doped $CeO_2(111)$. The effect of the U parameter on ΔE_V is small for most of the dopants (ca. 0.1 eV), with Ir and Au being the exceptions where ΔE_V becomes slightly negative for Au, too (Table S2). Our results differ from the previous DFT studies. For the metals considered in this study, Shapovalov et al. [44] reported ΔE_V to be negative for Cu, Ag, and Au (without using DFT+U), while Krcha et al. [18] reported that ΔE_V was negative for Ag and Au only and positive for the other metals. Table 1 summarizes the calculated minimum ΔE_V for vacancy formation at different locations with each dopant atom.

Table 1. Calculated formation energies (ΔE_V , in eV) of surface oxygen vacancy (V_O^S) and sub-surface oxygen vacancy (V_O^{SS}) at the nearest neighbor (NN) and next nearest neighbor (NNN) positions on M-doped CeO₂(111), where M = Co, Rh, Ir, Ni, Pd, Pt, Cu, Ag, and Au.

Group	Dopant	$\Delta E_{\rm V} ({\rm eV})$		$\Delta E_{\rm V} ({\rm eV})$	
		$V_{\mathrm{O}}{}^{\mathrm{S}}$	$\mathrm{Vo}^{\mathrm{SS}}$	$ m V_{O}{}^{S}$	${\rm V_{\rm O}}^{\rm SS}$
		(NN)	(NN)	(NNN)	(NNN)
	un-doped	+2.93	+2.77	-	-
9	Co	+0.68	+1.01	+1.63	+1.28
	Rh	+0.44	+0.69	+1.25	+1.07
	Ir	+1.06	+1.31	+1.87	+1.79
10	Ni	-0.43	-0.20	+0.50	+0.20
	Pd	-0.62	-0.39	+0.16	-0.01
	Pt	-0.06	+0.15	+0.73	+0.62
11	Cu	-0.17	+0.09	+0.71	+0.35
	Ag	-0.18	-0.03	+0.46	+0.28
	Au	+0.43	+0.68	+1.25	+1.10

 $\Delta E_{\rm V}$ is calculated based on the minimum-energy stoichiometric surface, $V_{\rm O}{}^{\rm S}$, and $V_{\rm O}{}^{\rm SS}$ respectively for each dopant as indicated in Figures 1 and 3 with respect to ${}^{1}\!\!/_{\!2}O_{2(g)}$.

For un-doped $CeO_2(111)$, ΔE_V of V_O^S reported here is in agreement with literature values calculated using a similar U value [45]. V_O^{SS} is 0.16 eV more stable than V_O^S , in agreement of Ganduglia-Pirovano et al. who reported V_O^{SS} to be more stable than V_O^S by 0.12 eV using PBE+U with U=4.5 eV [36]. Other theoretical as well as experimental studies have also concluded that V_O prefers to be located in the sub-surface (3rd atomic) layer in $CeO_2(111)$ [46, 47]. In contrast,

all of the dopant metals favor the formation of V_O^S over V_O^{SS} at an NN position. The difference in ΔE_V between NN V_O^S and V_O^{SS} does not vary substantially for metal to metal, being approximately 0.15~0.35 eV in favor of V_O^S . For a detailed account of our findings for NN V_O^{SS} formation and for NNN V_O^S and V_O^{SS} formation, please see SI. Table 1 suggests that the field of influence of the dopant atom decays rapidly with distance.

The square planar structure is highly prevalent among the nine dopant metals, whether as part of a stoichiometric surface or V_0 . Krcha et al. reported doped V_0^S to adopt a square planar structure for Rh, Ir, Pt, Ag, and Au, whereas V_0^S doped with Co, Ni, and Pd prefers a pyramidal structure [18]. Nolan performed both GGA-PW91 (with U=5 eV applied to Ce 4f) and HSE06 calculations using (2×2) surface unit cells and reported that Pd- and Ni-doped V_0^S form square planar structures [19]. Carey et al. also reported Cu doped into CeO₂(111) to adopt a square planar configuration with a $\Delta E_V = -0.64$ eV with a (4×2) surface unit cell using GGA-PBE (with U=5 eV applied to Ce 4f and 7 eV to Cu 3d) [48]. We find the alternate structures to be generally much higher in energy than the square planar structure. For the 4d and 5d metal dopants in Groups 10-11, the rectangular pyramidal structure (Figure 2a) relaxes into the rectangular planar structure (Figure 2b) by losing the coordination between the dopant atom and the O atom in the 4th atomic layer beneath them. Neither rectangular structure is stable for the 3d metal dopants.

Experimentally, to obtain detailed information on the local coordination geometry of singly dispersed dopant atoms in ceria is not trivial and requires careful analysis using X-ray absorption spectroscopy. Such evidence has been scant in the literature in the past but is growing. Dvořák et al. concluded based on photoelectron spectroscopy, scanning tunneling microscopy, and DFT calculations that Pt single atoms are stabilized by monoatomic step edges on ceria as Pt²⁺ in planar

PtO₄ moieties [49]. Resasco et al. [7] proposed based on multiple experimental methods that after oxidation at 300 °C in 5% O₂, dispersed Pt atoms exist on ceria in a +4 oxidation state with sixfold coordination with oxygen atoms, and when ceria is reduced at 250 °C in 5% H₂, Pt adopts a +2 oxidation state and fourfold coordination in a square planar geometry. They reported an average Pt-O bond distance of 2.02±0.04 Å after oxidation and 2.01±0.03 Å after partial reduction. We calculate the average Pt-O bond distance to be 2.14±0.03 Å (Figure S1h) and 2.01±0.02 Å (Figure S2h) in the respective corresponding structures. Single-atom Pt²⁺ species in square planar PtO₄ moieties was also reported by Jiang et al. [8]. Bera et al. combusted mixed Ce and Cu precursor solutions at ca. 1000 °C to prepare 3-10 at% Cu-CeO₂ samples and characterized them using EPR, XPS, and XANES [50]. They reported Cu to be in the +2 state with oxygen vacancy formation around the Cu ions. The first coordination shell was determined to contain 3.14 O atoms at 1.96 Å. In a more recent study on Cu-doped ceria catalysts by García-Vargas et al., the first shell coordination and bond distance were calculated to be 2.74 O atoms and 1.95 Å based on EXAFS [51]. The minimum energy Cu-doped V_O^S structure that we have found (Figure S2c) has CN=4 with an average Cu-O distance of 1.95 Å. The precise location of the dopant atoms was not known in most of these studies.

Chemically, any metal atom should enter into a formal oxidation state of +4 when placed at a cation site in a stoichiometric CeO₂ lattice. As Krcha et al. pointed out [18], since none of the dopant elements considered in this study prefers to go above an oxidation state of +4, they cannot reduce Ce. Also, all nine metals have higher ionization potentials (1st through 4th) than Ce in the gas phase, so they do not prefer to be in the +4 oxidation state as much as Ce. One way to accommodate a dopant metals in the preferred oxidation state is to remove a O_{latt} atom, thereby releasing the electrons that are tied up by the oxygen to the dopant atom. This has been termed

"charge compensating oxygen vacancies" [19, 52, 53]. It is therefore reasonable to expect the removal of O from ceria to be less energetically costly upon substitutional doping with the metals. According to Krcha et al., upon Vo^S formation Au and Co adopt a +3 oxidation state and Ir remains in a +4 oxidation state, while the rest of the metals considered here take on a +2 oxidation state. We have performed the Bader charge analysis to determine the charge distribution in the V_0^S configurations for each dopant metal (Table S2). In the minimum-energy V_0^S configurations doped with Ni, Pd, Pt, Cu, and Ag, the excess electrons associated with the oxygen vacancy are not found on any of the Ce atoms (i.e., no Ce³⁺ species), implying that the dopant atoms are in a (+4) + (-2) = +2 oxidation state. For the Co-, Ir-, and Au-doped V_0^S , a single NNN Ce is reduced to +3 (i.e., taking on the same amount of additional charge as by one of two Ce atoms in V_0^{SS} in un-doped V_0^S , the two lowest spin states are less than 0.1 eV apart, with the ground state (doublet) being in a +2 oxidation state while the other being in a +3 oxidation state. Our results regarding the oxidation state of the dopant metals agree with what Krcha et al. reported [18].

The prevalence of the square planar structure mirrors the preference for the same structure by molecular TM complexes involving some of the same metal cations as considered here. It is well known that only metal atoms or cations with a low-spin d^8 configuration form square planar complexes. Those with fewer or more d electrons usually form octahedral or tetrahedral complexes instead. Ni²⁺, Pd²⁺, Pt²⁺ and Au³⁺ all have d^8 configurations, which naturally form square planar complexes. Those elements with more than eight d electrons in the neutral state are capable of adopting a d^8 configuration (e.g., Cu²⁺ as s^1d^8 instead of s^0d^9). The Group 9 elements (Co, Rh, Ir) have fewer than eight d electrons, which favors the octahedral structure over the square planar structure. However, when situated at the ceria surface, these dopant atoms cannot achieve

necessary bonding with eight lattice oxygen atoms simultaneously because of the broken symmetry at the surface and because of the fact that the O_{latt} atoms are constrained by the crystal lattice. By forgoing ligation along the z axis, the dopant atom can relax instead into the square planar structure where bonding with four O_{latt} atoms at less than 2 Å can be established.

3.3 O₂ adsorption in oxygen vacancy

Since the dopant metals considered in this study all favor the formation of V_0^S to V_0^{SS} , at NN instead of NNN locations, we examine O_2 adsorbed in the doped NN V_0^S structures considered above, including rectangular pyramidal, square planar, and trigonal planar (Figure 3a-f). With the square planar V_0^S structure, it is furthermore possible for the O_2 moiety to stably adopt different orientations, including one in which it is not in direct contact with the dopant atom. The adsorption energy of O_2 in the different configurations is plotted in Figure 3g.

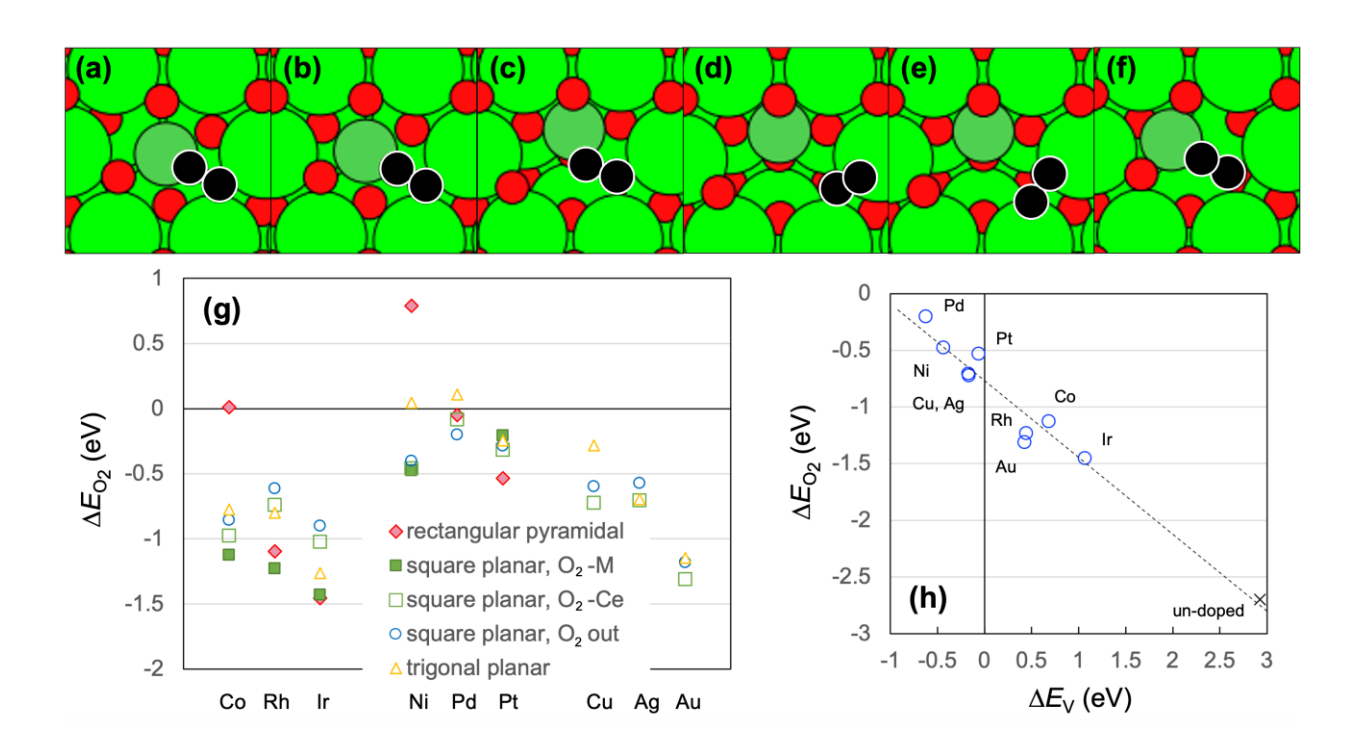


Figure 3: Configurations of O_2 (shown as black circles) adsorbed in doped V_O^S of different structures on $CeO_2(111)$: rectangular pyramidal (a) involving two O atoms in the 3^{rd} atomic layer and one O atom in the 4^{th} atomic layer (Co, Rh, Ir) or (b) involving three O atoms in the 3^{rd} atomic layer (Pd, Pt); square planar (c) with O_2 in contact with the dopant atom (O_2 -M), (d) with O_2 not in contact with the dopant atom (O_2 -Ce), or (e) with O_2 out of the vacancy (O_2 out); (f) trigonal planar. (g) Adsorption energy of O_2 (ΔE_{O_2} , all referenced to the minimum-energy V_O^S as indicated in Figure 2) adsorbed in the various doped V_O^S configurations. (h) Minimum ΔE_{O_2} from (g) vs. oxygen vacancy formation energy (ΔE_V) on each surface. The line is the result of linear regression: y = -0.68x - 0.77, drawn as a guide to the eye; same below. Snapshots of the actual minimum-energy O_2/V_O^S structure for each dopant are shown in Figure S3 in SI. See Table S3 for the data plotted in (h).

The minimum-energy configuration for $O_2/V_O{}^S$ involves the square planar $V_O{}^S$ (Figure 3c-f) for all of the dopants except for Ir (Figure 3a) and Pt (Figure 3b), which involves the rectangular pyramidal $V_O{}^S$ instead. O_2 prefers to contact C_O , Rh, Ir, Ni, and Pt thereby increasing $C_O{}^S$ to 5 ($C_O{}^S$, Rh, and Ni) and 6 (Ir and Pt), while Pd and the Group 11 dopant atoms prefer $C_O{}^S$ without contacting $O_D{}^S$. Here $O_D{}^S$ is considered to be in contact with a dopant atom if the distance between the dopant and either of the O atoms is less than 2.2 Å. For the Group 11 dopants ($C_O{}^S$, and Au), the rectangular pyramidal structure relaxes into the trigonal planar structure by giving up coordination to two O atoms in the 0-f atomic layer, while the square planar 0-f configuration relaxes with the $O_D{}^S$ moiety losing contact with the dopant atom. In the end, no stable high-valence (i.e., $C_O{}^S$) configuration can be found for the Group 11 dopants. When plotted against 0-f including 0-f configuration can be found for the Group 11 dopants. When plotted against 0-f including 0-f configuration can be found for the Group 11 dopants. When plotted against 0-f including 0-f interacts with 0-f via an oxygen atom. The weakest interaction with 0-f occurs with Pd-dosed 0-f corresponding to the most exothermic 0-f and Pt should

maximize the amount of vacancy-stabilized O_2 species formed on $CeO_2(111)$, by striking a balance between $V_O{}^S$ concentration and O_2 adsorption.

The O-O bond length (do-O), O-O vibrational frequency (vo-O), and Bader charge of the adsorbed O₂ species are plotted for the minimum-energy and 2nd minimum-energy O₂/Vo^S states as reported in Figure 3, in Figure 4. An approximately linear relationship is observed between the bond length (do-O) and vibrational frequency (vo-O) of these O₂/Vo^S states (Figure 4a). The vo-O value divides the O₂ species into three groups: gas-phase (1555 cm⁻¹), superoxide (1100~1200 cm⁻¹), and peroxide (< 1000 cm⁻¹). In terms of do-O, the boundary between the superoxide and peroxide states is 1.35~1.36 Å. Of all the O₂ states we have investigated (Figure 3), with rare exceptions, all of the peroxide states occur in the high-valence configurations (filled symbols in Figure 3g), while all of the superoxide states occur with the dopant atoms having CN=4 (open symbols in Figure 3g). The minimum-energy O₂ state is peroxide for all the Group 9 dopants and Pt, which illustrates the trend that the higher-valance states become more favored as the dopant comes from farther left of the periodic table. It also tracks the maximum coordination of the metal atoms to oxygen (cf. the metal elements in their native oxides), which generally increases as one moves farther to the left of the periodic table.

On un-doped $CeO_2(111)$, we obtain 890 cm⁻¹, 1.44 Å, and -1.19 electrons for the minimum-energy $O_2/V_O{}^S$ state in which the outer O is in contact with one Ce cation, and a slightly less stable state with 929 cm⁻¹, 1.45 Å, and -1.23 electrons in which the outer O is in contact with two adjacent Ce cations (both included in Figure 4). These results are in line with the overall trends and are in close agreement with previously reported DFT+U results for $O_2/V_O{}^S$ on un-doped $CeO_2(111)$ [37, 47, 54-57].

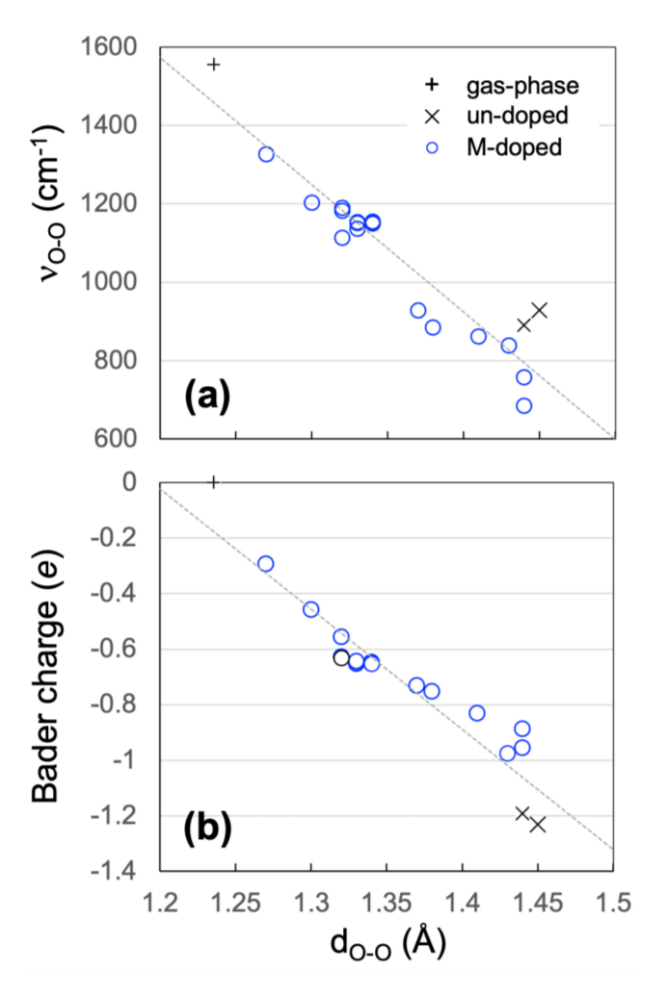


Figure 4: (a) O-O vibrational frequency (v_{O-O}) and (b) Bader charge plotted against the O-O bond length (d_{O-O}) of various O_2 states adsorbed in V_O^S on un-doped and doped $CeO_2(111)$. Values for gas-phase O_2 are included for comparison. The lines are the results of linear regression: in (a), y = -3236x + 5455; in (b), y = -4.368x + 5.224. See Table S4 for the data plotted. All results shown in this figure are calculated for structures re-optimized with U=5 eV.

The Bader charge also closely correlates with d₀₋₀ on each surface, so that more excess charge results in a longer O-O bond (Figure 4b). All of the O₂ species acquire excess charge and are therefore anionic. The Bader charges are fairly evenly distributed without any clear demarcation between the superoxide and peroxide states, as opposed to in Figure 4a. An analysis of the electronic structure should provide a more reliable theoretical basis than the Bader charges

on which to distinguish between the superoxide and peroxide states (see, e.g., Figure S4, which illustrates extensive hybridization of the oxygen frontier $1\pi_u$ orbitals with the dopant d states in the peroxide states, but not in the superoxide states). Whether O_2/Vo^S prefers to be in a superoxide or peroxide state is ultimately determined by how readily the dopant atom, as it is incorporated into the V_O^S structure, is able to hybridize with the O_2 orbitals.

The results here do not rule out the possibility that facets other than (111), different types of defects, or surface adsorbates due to a reactive environment, can produce prevailing O_2 states on ceria nanomaterials [47, 54, 57-60] that are different from the minimum-energy states reported here. No stable O_2 state can be detected on a defect-free $CeO_2(111)$ surface [47]. Since the dopants enhance the reducibility of $CeO_2(111)$, we conclude that stable O_2 cannot form on defect-free doped $CeO_2(111)$ either since O_2 adsorption would amount to further oxidation of the surface. Therefore, O_2 without V_O^S is not considered.

Incidentally, the lone Ce^{3+} species that accompanies the Co-, Rh-, and Au-doped Vo^S disappears, presumably taken up by the O₂. It persists after O₂ adsorption in the Ir-doped Vo^S, which suggests the Ir atom is formally further oxidized to a +5 oxidation state. The Bader charge of a dopant atom in the minimum-energy O₂/Vo^S configurations turns out to be essentially identical to that of the same dopant atom in the minimum-energy stoichiometric site for all of the dopants except Ir and Pd (Table S5). If this is taken to indicate that the dopant atom is in the same oxidation state in the two structures, then, for Ni, Cu, Ag, and Au for which the O₂/Vo^S is a superoxide, the dopant should be in a +3 oxidation state together with an oxygen hole [61, 62] in the stoichiometric site, while Co, Rh, and Pt, for which the O₂/Vo^S is a peroxide, are reaffirmed by this reasoning to be in a +4 oxidation state as we have assumed in the last section. Indeed, an electron hole in the form of notably reduced Bader charge is found to be located on one of the O_{latt}(-Ce) sites in the

stoichiometric square planar structure (see Figure 5a for designation) for Ni, Cu, Ag, and Au, but not for the other dopants.

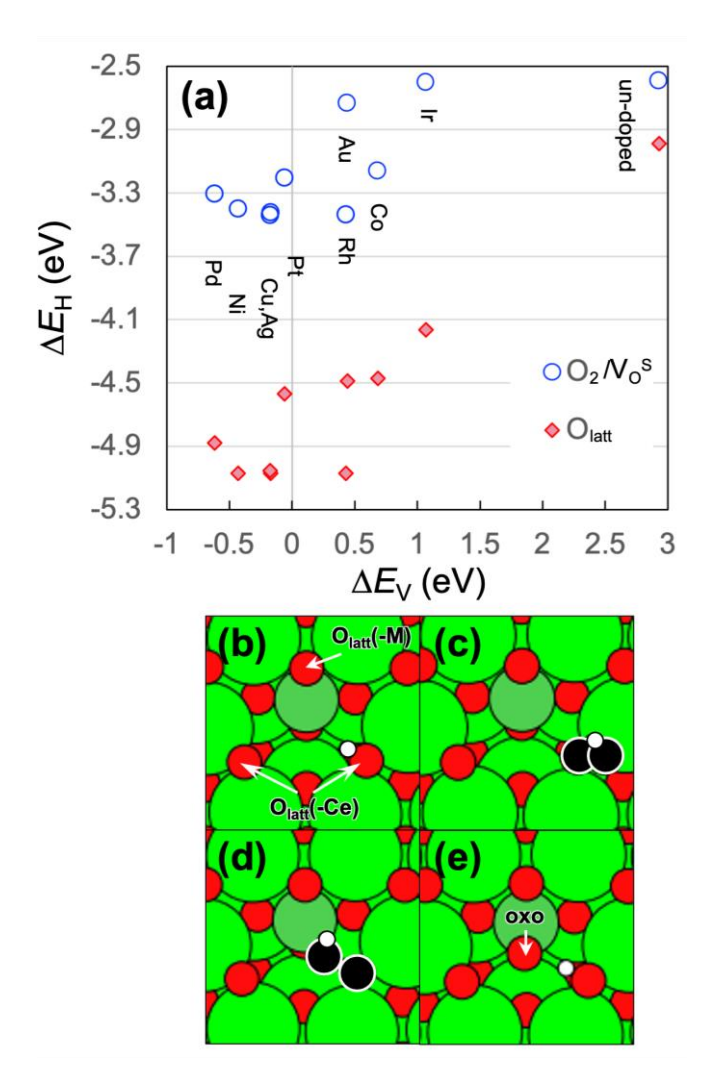


Figure 5: (a) Minimum O-H bond energy ($\Delta E_{\rm H}$, with respect to a gas-phase H atom) vs. oxygen vacancy formation energy ($\Delta E_{\rm V}$) on un-doped and doped CeO₂(111). Snapshots of different H adsorption configurations in (a): (b) H adsorption on O_{latt}(-Ce); H adsorption on O₂/V_O^S with H on O₂ (c) not in contact with the dopant atom or (d) in contact with the dopant atom, and (e) with O-O bond scission forming an OH in V_O^S and an oxo species. (b-d) are all based on the square planar V_O^S (Figure 2d). O₂ moiety is shown as black circles. See Table S6 for the data plotted in (a).

3.4 Hydrogen adsorption on reactive oxygen species

As shown above, multiple types of reactive oxygen species (ROS) can be found in the vicinity of a dopant atom on CeO₂(111), including inequivalent lattice oxygen atoms (O_{latt}) and O₂ stabilized by a surface oxygen vacancy (O₂/V_O^S). Next, we consider the adsorption of atomic H, the simplest reductant, on these ROS. Reduced ceria promotes the population of hydride states (Ce-H) [63, 64], which are much less stable than O_{latt}-H and are not the subject of this study. The calculated minimum O-H bond energy ($\Delta E_{\rm H}$) for the ROS species connected with each dopant metal is plotted in Figure 5a. For reference, $\Delta E_{\rm H}$ is -2.99 eV on O_{latt} and -2.60 eV on O₂/V_O^S on un-doped CeO₂(111), in agreement with the literature [35, 45]. $\Delta E_{\rm H}$ is distributed across -3.2 ~ -5.1 eV, many of which are considerably more exothermic than on un-doped CeO₂(111). A loose positive correlation between $\Delta E_{\rm H}$ and $\Delta E_{\rm V}$ can be discerned.

For H bonded to O_{latt} , we consider the two non-equivalent O_{latt} (-Ce) sites and one that is bonded to the dopant atom (O_{latt} (-M); see Figure 5a) in the square planar structure. In all cases, ΔE_{H} is considerably more exothermic for H bonded to O_{latt} (-Ce) than to O_{latt} (-M) (cf. Table S6). This is consistent with how the minimum-energy V_{O}^{S} is also located at the O_{latt} (-Ce), not O_{latt} (-M) site of the doped square planar structure (Figure 2d). For the Pd- and Pt-doped stoichiometric surfaces, H adsorbed on O_{latt} in the octahedral structure (all three NN O_{latt} atoms being equivalent, cf. Figure 1a) turns out to be much higher in total energy than H adsorbed on O_{latt} (-Ce) in the square planar structure, so the latter is considered below. This implies that H adsorption may induce a local geometric rearrangement for the Pd- and Pt-doped CeO₂(111).

The minimum O-H bond energies for the 2nd and 3rd H adsorbed on the doped sites are plotted in Figure S5. It can be seen that hydrogen adsorption becomes less exothermic with the

local H coverage and approaches that on un-doped $CeO_2(111)$ when all three O_{latt} sites NN to the dopant atom are occupied. The notable exception is Ag.

states, which represents the maximum oxidative power of the O_2 state. For all the dopant metals except Ir, the minimum-energy hydrogenated O_2 states occur in the square planar $V_O{}^S$. For Ir it occurs in the rectangular pyramidal $V_O{}^S$ as is $O_2/V_O{}^S$. For the Groups 10-11 dopants, a molecular OOH state is preferred that is not in direct contact with the dopant atom (Figure 5c). For the peroxide O_2 in Co-, Rh-, and Ir-doped $V_O{}^S$, hydrogenation at the O atom closer to the dopant atom results in a molecular OOH state (Figure 5d), whereas hydrogenation at the other O atom results in the spontaneous rupture of the O-O bond forming an apical oxo group on the dopant atom plus an OH group occupying the $V_O{}^S$ (Figure 5e). It is clear from Figure 5a that $O_2/V_O{}^S$ is less reactive an ROS than $O_{latt}(-Ce)$. The energetically preferred adsorption sites for additional H atoms in the presence of $O_2/V_O{}^S$ are the remaining $O_{latt}(-Ce)$ and $O_{latt}(-M)$ sites and not the O_2 , except for the Group 9 dopants (Figures S6).

3.5 Reaction energetics of H₂ oxidation

The results above are used next to analyze the energetics of the oxidation of H_2 and propane (C_3H_8). We defer a detailed study of the mechanisms of these reactions to future work. Here we analyze the energetics of simplified catalytic cycles for these reactions to illustrate a key idea. For H_2 oxidation, the cycle may consist of the following steps for a dopant with $\Delta E_V > 0$:

$$H_2 + 2O/V \rightarrow 2HO/V \tag{i}$$

$$2HO/V \rightarrow H_2O + V + O/V$$
 (ii)

$$O_2 + V \rightarrow O_2/V$$
 (iii)

$$H_2 + 2O/V \rightarrow 2HO/V \text{ (w. O}_2/V \text{ or } O^* + O/V)$$
 (iv)

$$2HO/V + O_2/V \text{ (or } O^* + O/V) \rightarrow H_2O + 3O/V$$
 (v)

Here V_0^S is further abbreviated to V for clarity. It is in line with the general mechanism proposed by Vannice for oxide catalysts, in which the active site is a lattice vacancy that accommodates either O_{latt} or O_2 , both of which being capable of reacting with the reductant [65]. In keeping with this notion, O_{latt} and O_2 adsorbed in a vacancy are denoted in the equations above as O/V and O_2 /V, respectively, and adsorbed H as HO/V. The energy profiles for the proposed reaction steps are plotted in Figure 6a-b. The minimum-energy 2H and 2H+ O_2 /V states for each dopant (shown in Figures S5 and S6) are used to make Figure 6a-b. The overall reaction is $2H_2 + O_2 \rightarrow 2H_2O$, with $\Delta E = -5.15$ eV, or -2.57 eV/ H_2 according to GGA-PW91.

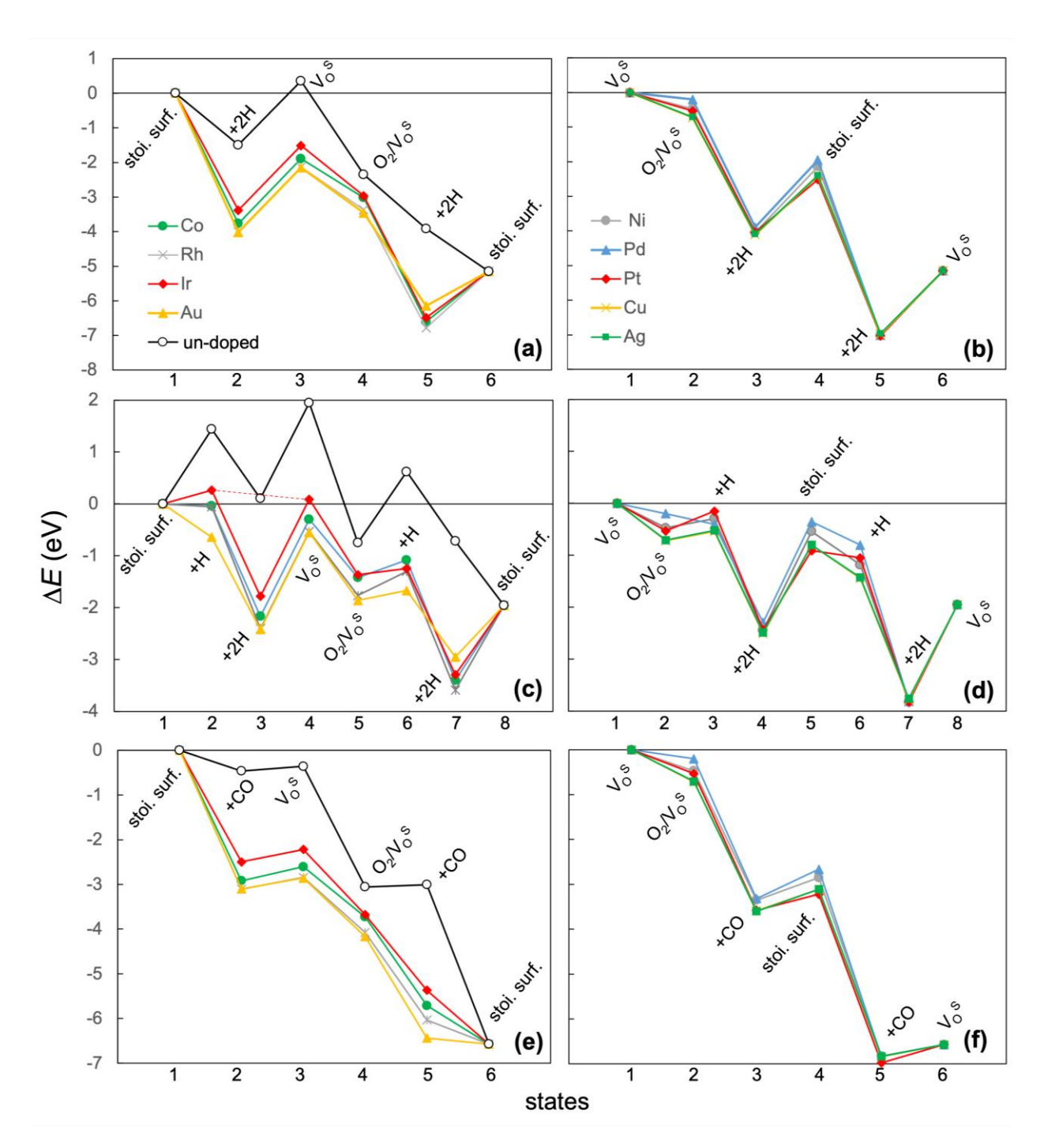


Figure 6: Reaction energy profiles for the oxidation of H_2 , C_3H_8 , and CO on un-doped and doped $CeO_2(111)$. The reactants are one gas-phase O_2 and (a,b) two H_2 , (c,d) two C_3H_8 , and (e,f) two CO. (a,c,e) are for dopants with $\Delta E_V > 0$; (b,d,f) are for dopants with $\Delta E_V < 0$ (cf. Table 1). The states of the surface along a reaction path are as labeled; gas-phase species and O_{latt} are omitted from labels for brevity.

For dopants with $\Delta E_{\rm V} > 0$, the catalytic cycle begins with ${\rm H_2}$ dissociative adsorption (Step i). For a dopant with $\Delta E_{\rm V} < 0$, the cycle begins with ${\rm V_0^S}$ (Step iii) and goes through the same sequence of steps, with Step i following Step v. Previous theoretical studies put the activation barrier (E_a) for ${\rm H_2}$ dissociation on un-doped ${\rm CeO_2(111)}$ at $0.8 \sim 1.3$ eV depending on the value of U and whether the dissociation is heterolytic or homolytic [45, 64, 66, 67]. The dopants make Step i more exothermic than on un-doped ${\rm CeO_2(111)}$, with ΔE in a strong correlation with $\Delta E_{\rm V}$ (Figure 7). A similar strong correlation exists for Step iv (see Figure S7). Based on the Bronsted-Evans-Polanyi relation, it is expected that E_a for ${\rm H_2}$ dissociation decreases correspondingly with doping. Sample calculations on the un-doped and some doped (Co, Ni, and Pt) sites confirm this (see Figure S8).

Regardless of the specific mechanism by which H_2 is activated on $CeO_2(111)$ [66, 67], the dissociated H atoms are eventually accommodated by a pair of O_{latt} sites. All the steps have $\Delta E < 0$ on the un-doped surface except for Step ii (#2 \rightarrow #3 in Figure 6a), which is significantly endothermic by 1.85 eV. Step ii is commonly referred to as surface reduction since an oxygen vacancy is physically created, although, in the Lewis sense, the reduction of the surface occurs upon the initial adsorption of H, whereas the extent of surface reduction is the same through Step ii: Both the reactant and the product states of this step involve similar dopant structures, two excess electrons, and the same number of O-H bonds. This accounts for why Step ii has a nearly constant ΔE of ca. +1.8 eV on the un-doped and doped sites (#2 \rightarrow #3 in Figure 6a; #5 \rightarrow #6 in Figure 6b). We term Step ii an "iso-reduction" step. It is fundamentally different from simply removing an O atom from a stoichiometric $CeO_2(111)$ surface to create a V_0 , during which the surface *becomes* reduced. Hansen et al. calculated that the decomposition of two hydroxyls forming water on un-

doped CeO₂(111) has an E_a that is just slightly larger than the ΔE [45], based on which we hypothesize likewise $E_a \approx \Delta E$ for Step ii on the doped sites.

 $V_O{}^S$ is re-oxidized by O_2 and not re-filled through the migration of lattice oxygen because the latter would amount to a counter-diffusion of $V_O{}^S$ away from the doped site, which is highly unfavorable (Table 1), whereas $O_2{}^S$ adsorption in $V_O{}^S$ is exothermic in all cases. The dissociative adsorption of another $H_2{}^S$ molecule yields $O_2{}/V_O{}^S$ co-adsorbed with two H atoms except for $C_O{}^S$, Rh, and Ir, for which $O_2{}^S$ prefers to dissociate (see Figure S6). Removal of the second set of H atoms and half of the $O_2{}^S$ restores the stoichiometry of the surface. This surface re-oxidation step (Step v) has a varying $\Delta{}^S$ that is more endothermic with more negative $\Delta{}^S$, being the lowest at -1.24 eV on un-doped $C_O{}^S$ (111) and slightly exceeding +1.9 eV with Ni and Pd. $\Delta{}^S$ of the three key steps (Steps i, ii, and v) is plotted against $\Delta{}^S$ (Figure 7) to better illustrate the energetic feature of these step.

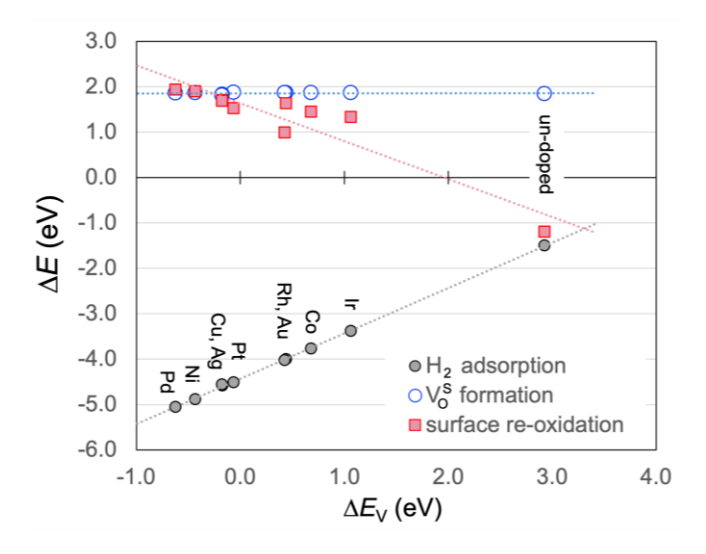


Figure 7: ΔE for H₂ dissociative adsorption (Step i), V_O^S formation (Step ii), and surface reoxidation (Step v) vs. oxygen vacancy formation energy (ΔE_V). The lines are the results of linear regression: H₂ adsorption: y = 1.00x - 4.43; V_O^S formation: y = 0.00x + 1.86; surface re-oxidation: y = -0.83x + 1.64.

Overall, H_2 oxidation cannot catalytically turn over on $CeO_2(111)$ until a sufficient temperature is reached to permit removal of H as H_2O . Surface reduction peaks have been reported above 720 K in H_2 temperature programmed reduction over polycrystalline ceria [12, 68]. Désaunay et al. investigated H_2 oxidation on octahedral ceria nanoparticles that exhibit $CeO_2(111)$ predominantly and reported a peak temperature of ca. 930 K. An apparent E_a of 150 kJ/mol was fitted to their data, although the authors acknowledged the presence of impurities of more reactive ceria nano-rods [69]. The H_2 consumption pattern in the H_2 TPR study by Bera et al. [50] showed that H_2 uptake began at around 200 °C and increased slowly until peaking at 600 °C, which supports the interpretation that the reaction is limited by hydrogen exiting the surface. Doping affects ΔE and E_a of H_2 dissociative adsorption, which would permit a larger forward reaction flux than on un-doped $CeO_2(111)$. However, ΔE for Step ii remains much larger than E_a of Step i and any possible effects of doping on it. Doping ceria is therefore concluded to be ineffective at promoting the catalysis of this reaction owing to the iso-reduction step (Step ii) being rate-limiting over a wide range of ΔE_V .

3.6 Reaction energetics of C_3H_8 partial oxidation

Previous theoretical studies suggest that the O-H bond energy plays a direct role in the activation of C-H bonds by an oxyanion species [18, 70-72]. The fact that certain $|\Delta E_{\rm H}|$ values in Figure 5a exceed the calculated C-H bond energy of methane (4.81 eV) suggests that doped CeO₂(111) may be reactive enough to activate hydrocarbons under mild conditions. However, accelerating one step in a catalytic reaction does not guarantee that the overall reaction is accelerated. Here we

consider the partial oxidation of C_3H_8 , the smallest hydrocarbon with a secondary C-H bond, to C_3H_6 . It takes two molecules of propane to balance one O_2 : $2C_3H_8 + O_2 \rightarrow 2C_3H_6 + 2H_2O$, with $\Delta E = -1.95$ eV, or -0.98 eV/ C_3H_8 . We postulate a mechanism involving successive hydrogenation by a secondary H atom and then a primary H atom, i.e., for a dopant with $\Delta E_V > 0$:

$$C_3H_8 + O/V \rightarrow C_3H_7 + HO/V \tag{i'}$$

$$C_3H_7 + O/V \rightarrow C_3H_6 + HO/V \text{ (w. HO/V)}$$
 (ii')

$$2HO/V \rightarrow H_2O + V + O/V \tag{iii'}$$

$$O_2 + V \rightarrow O_2/V$$
 (iv')

$$C_3H_8 + O/V \rightarrow C_3H_7 + HO/V \text{ (w. O}_2/V \text{ or O}^* + O/V)$$
 (v')

$$C_3H_7 + O/V \rightarrow C_3H_6 + HO/V$$
 (w. HO/V and O_2/V or $O^* + O/V$) (vi')

$$2HO/V + O_2/V \text{ (or } O^* + O/V) \rightarrow H_2O + 3O/V$$
 (vii')

For a dopant with $\Delta E_{\rm V} < 0$, the cycle begins with a vacancy (Step iv') and goes through the same sequence of steps. A secondary H atom in C₃H₈ is 2.16 eV more stable than ½ H₂, while a primary H atom in iso-propyl (i-C₃H₇) is 0.56 eV less stable than ½ H₂. Thus, ΔE of those steps that involve a secondary H (#1 \rightarrow #2 and #5 \rightarrow #6 in Figure 6c, #2 \rightarrow #3 and #5 \rightarrow #6 in Figure 6d) is less exothermic than ΔE of the steps involving a primary H (#2 \rightarrow #3 and #6 \rightarrow #7 in Figure 6c, #3 \rightarrow #4 and #6 \rightarrow #7 in Figure 6d). The reaction energetics on all the doped sites are similar, being more favorable than on the un-doped surface. In particular, ΔE for the initial H abstraction from C₃H₈ (Step i') is significantly more exothermic than on un-doped CeO₂(111), suggesting that the kinetics of activating C₃H₈ is enhanced by the dopants. This is confirmed with sample calculations on the un-doped and some doped (Co, Ni, and Pt) sites (see Figure S8), which are modeled after our previous work on C₃H₈ oxidative dehydrogenation on mixed metal oxides [72, 73]. i-C₃H₇ dehydrogenation (Step ii') is taken to be essentially barrierless [72]. Either V_O^S formation (Step

iii') or surface re-oxidation (Step vii') remains the more endothermic amongst all the steps regardless of the dopant species with ΔE in +1.8 \sim +1.9 eV, identical to the case of H₂ oxidation.

The step-wise cleavage of a less reactive C-H bond followed by a more reactive C-H bond is a general pattern for all but the smallest hydrocarbons. It creates the possibility that a primary H is transferred directly to an existing HO/V and bypasses the ca. 1.8 eV energetic barrier to reduce the surface directly (see e.g., dashed line in Figure 6), although energetically it is much more favored for a primary H to go to an open O_{latt} site. For comparison, Chen et al. dosed CeO₂(111) with atomic D and observed D₂O formation at as low as 200 K, which the authors interpreted as atomic D directly adsorbing onto existing DO/V forming D₂O [74]. Otherwise, atomic H would persist on the surface until sufficiently high temperatures where H₂O can evolve as in the case of H₂ oxidation, which hinders total oxidation at low temperatures. An alternate channel in which H can be removed from the surface is via small oxygenates (e.g., CH₂O), which represents incomplete combustion.

3.7 Reaction energetics of CO oxidation

CO oxidation by CeO₂(111) is considered next to contrast with H, because CO can remove lattice O upon unimolecular adsorption and CO₂ formation. This is also a major channel for carbon removal from the oxide surface in hydrocarbon oxidation. The overall reaction is $2\text{CO} + \text{O}_2 \rightarrow \text{CO}_2$ with $\Delta E = -6.57$ eV, or -3.29 eV/CO (N.B. the calculated value differs from the experimental ΔH of -2.9 eV by 0.4 eV). CO is capable of interacting with ceria in several states, including a weakly bound state over a cation site; a chemisorbed state bound to one O_{latt} atom that is equivalent to a CO₂ molecule located in V_O^S; and a state bound to two adjacent O_{latt} atoms forming a carbonate

species (CO₃) [33, 75-77]. Here we focus on chemisorbed CO as the key intermediate (see SI for more detail). We propose the main steps to be:

$$CO + O/V \rightarrow CO_2/V$$
 (i")

$$CO_2/V \rightarrow CO_2 + V$$
 (ii")

$$O_2 + V \rightarrow O_2/V$$
 (iii")

$$CO + O/V \rightarrow CO_2/V \text{ (w. } O_2/V \text{ or } O^* + O/V) \text{ (iv")}$$

$$CO_2/V + O_2/V \rightarrow CO_2 + 2O/V$$
 (v")

Again, for a dopant with $\Delta E_{\rm V} < 0$, the cycle begins with ${\rm O}_2$ filling an oxygen vacancy (Step iii") and goes through the same sequence of steps. Step ii" is ${\rm V}_{\rm O}$ formation (#2 \rightarrow #3 in Figure 6e and #5 \rightarrow #6 in Figure 6f) and Step v" is surface re-oxidation (#5 \rightarrow #6 in Figure 6e and #3 \rightarrow #4 in Figure 6f). Step v" may occur via ${\rm O}_2$ attack on the C center, or ${\rm CO}_2$ desorption followed by ${\rm O}_2$ annihilation of both vacancies.

When ΔE of these steps is plotted against $\Delta E_{\rm V}$ (Figure 8), a pattern similar to Figure 7 emerges. ΔE of ${\rm V_O}$ formation (Step ii") is also independent of the dopant species. This is intriguing due to the dissimilarities between H and CO. It can be understood as CO chemisorption on ceria surfaces has also been experimentally detected and theoretically calculated to reduce ${\rm Ce}^{4+}$ to ${\rm Ce}^{3+}$ [33, 75, 76]. By combining with an ${\rm O_{latt}}$ atom to form a closed-shell ${\rm CO_2}$, two electrons are formally released back to the oxide lattice in State #2 (Figure 6e), which involve essentially identical C-O bonding as in State #3 (the same holds for States #5 and #6 in Figure 6f). Thus, Step ii" is also an iso-reduction step. As in the case of Step ii for ${\rm H_2}$ oxidation, we surmise Step ii" to have $E_a \approx \Delta E$. Also as in the previous cases, surface re-oxidation (Step v") is more endothermic for dopants with more negative $\Delta E_{\rm V}$, until its ΔE exceeds that of ${\rm V_O}$ formation for those dopants with exothermic $\Delta E_{\rm V}$ including Ni and Pd (Figure 8).

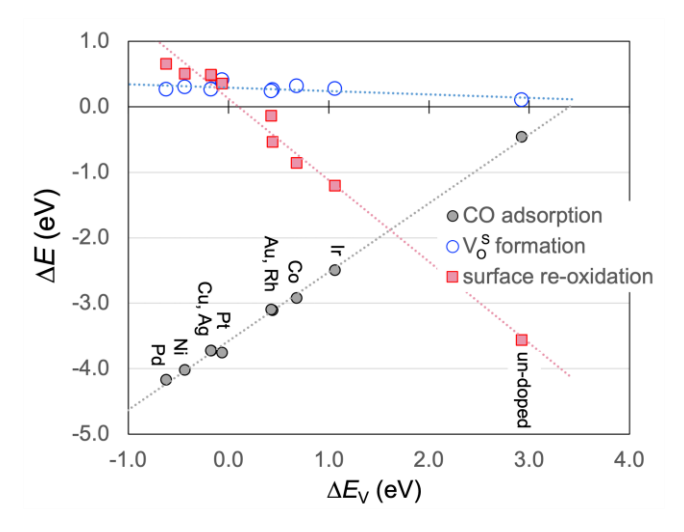


Figure 8: ΔE for CO chemisorption (Step i'), $V_O{}^S$ formation (Step ii'), and surface re-oxidation (Step v'') vs. oxygen vacancy formation energy (ΔE_V). The lines are the results of linear regression: CO chemisorption: y = 1.05x - 3.57; $V_O{}^S$ formation: y = -0.05x + 0.29; surface reoxidation: y = -1.25x + 0.13.

The dopants promote the adsorption of CO as they do with H_2 . As seen in Figure 8, ΔE for CO chemisorption (Step i', Figure 8) correlates almost perfectly linearly with ΔE_V . (A similarly strong correlation is found for Step iv", CO chemisorption in the presence of O_2 ; see Figure S7.) As before, more exothermic ΔE for Step i' is expected to correlate with smaller E_a for the step, which sample calculations on the un-doped and some doped (Co, Ni, and Pt) sites confirm (see Figure S8). Compared to H, the endothermicity of Vo formation by CO is much milder (Step ii", Figure 8), so that at the positive end of ΔE_V , CO chemisorption becomes the energetic bottleneck in the reaction. This key difference makes substitutional doping effective for promoting catalytic CO oxidation on $CeO_2(111)$. Experimentally, CO oxidation on polycrystalline ceria requires over 250 °C to light off [3, 4, 9, 10]. Dopants including Fe, Mn, Cu, Rh and Pd have been shown to lower the light-off temperature by $100\sim200$ °C [4, 9].

4 Conclusions

A theoretical study of $CeO_2(111)$ substitutionally doped with single atoms of the nine 3d-5d Groups 9-11 metals has been performed using periodic DFT calculations. All the metal dopants significantly reduce the energetic cost to create an oxygen vacancy (ΔE_V) compared to un-doped $CeO_2(111)$. The effect is most pronounced at lattice sites that are nearest-neighbor to a dopant atom and decreases with distance away from it. Ni, Pd, Pt, Cu, and Ag yield negative ΔE_V for a nearest-neighbor surface oxygen vacancy (V_O^S). A square planar structure is the local structure preferred in most cases by these dopants whether in a stoichiometric site, a surface oxygen vacancy, or a sub-surface oxygen vacancy. While O_2 does not stably adsorb on stoichiometric $CeO_2(111)$, doping the surface with these metals increases the likelihood of forming V_O^S and V_O^S -stabilized O_2 states. Based primarily on O-O bond length (< 1.35 Å or > 1.36 Å) and vibrational frequency (< 1000 cm⁻¹ or > 1100 cm⁻¹), the minimum-energy O_2 states in doped V_O^S are identified to be peroxides with Co, Rh, Ir, and Pt and superoxides with Ni, Pd, Cu, Ag, and Au.

Both lattice O atoms (O_{latt}) and $O_2/V_O{}^S$ species may extract hydrogen from organic compounds [78, 79]. To quantify the effect of doping, we have calculated the O-H bond energy (ΔE_H). ΔE_H for these two groups of reactive oxygen species (ROS) spans -3.2 ~ -5.1 eV, which is considerably more exothermic than on un-doped $CeO_2(111)$, with O_{latt} being more reactive toward H than $O_2/V_O{}^S$ is. The results are then used in the analyses of the energetics of representative catalytic oxidation reactions including H_2 and C_3H_8 . The more reactive O_{latt} species due to doping are expected to enhance the kinetics of H-H and C-H bond dissociation, which is only part of a catalytic cycle. The reactant and product states of H desorption as water producing an oxygen vacancy are chemically and structurally similar. Thus, ΔE of this key step, which is strongly

endothermic (ca. ± 1.8 eV) and much higher than calculated E_a for H₂ dissociative adsorption, is virtually unaffected by the elemental identity of the dopant. This step is therefore identified as the energetic bottleneck in the overall H₂ oxidation reaction. Total oxidation of hydrocarbons and other compounds such as HCl also produces adsorbed H that needs to be removed from the ceria surface, which should therefore be constrained at least in part by the same step, although alternate channels for removing H may exist in the other reactions.

Although CO interacts with the surface differently from H, the desorption of CO₂ producing an oxygen vacancy is likewise an iso-reduction step, so its energetics is also insensitive to the dopant species. Unlike H₂ oxidation, however, the dopants are predicted to have a notable promotional effect on CO oxidation because the iso-reduction step has a small $|\Delta E|$ and is not expected to pose a bottleneck. In this case, enhancing CO chemisorption boosts the overall reaction vs. un-doped CeO₂(111), while dopants like Ni and Pd causes the opposite problem where surface re-oxidation becomes the bottleneck.

The concept of an iso-reduction step is expected to hold regardless of the precise $\Delta E_{\rm V}$ values that individual dopant metals impart to ${\rm CeO_2(111)}$. It modifies the common view regarding the effect of doping on ceria catalysis, which holds that the optimal dopant is what achieves a balance between vacancy formation and surface re-oxidation. Instead, three key steps, i.e., chemisorption, ${\rm V_O}$ formation, or surface re-oxidation, need to be considered together. The straightforward framework presented here can be used readily to check if doping a ${\rm CeO_2(111)}$ facet, or another facet of ceria, or another oxide with a specific metal can be expected to intrinsically improve the catalysis of an oxidation reaction via the Mars-van Krevelen, or rather, the Vannice, mechanism.

Of course, doping ceria to modify catalytic activity is a complex issue. While this study attempts to quantify the chemical effects of doping on the formation and reactivity of ROS on CeO₂(111), it does not address the material feasibility of doping ceria with different metals. Different metals are not incorporated into the ceria lattice with equal ease. Some prefer to reside in the bulk of ceria while others prefer to be located in the surface region, and still others may form separate phases from ceria. Having a high concentration of the dopant atoms in the sub-surface layer of CeO₂(111) would generally be advantageous because it increases the availability of more reactive ROS than on un-doped CeO₂(111) and allows the dopant fields to overlap. What needs to be taken into account is that different metals have different energetic preferences for being located in the surface region vs. the bulk of ceria (see SI), so using the same precursor loadings in synthesis for different metals may not yield the same dopant concentrations in the surface. Furthermore, dopants may also modify the surface energies of ceria, posing challenges to creating stable nanoparticles of ceria of controlled sizes and shapes when doped with different metals [9]. All of these considerations will limit the available materials space in which researchers can design new, practical ceria-based catalysts.

Acknowledgments

This work was supported by the U.S. National Science Foundation under Grant No. CHE-2204075, and used high performance computational resources provided by Louisiana State University (hpc.lsu.edu) and by the National Energy Research Scientific Computing Center, which is supported by the Office of Science of US-DOE (under Contract No. DE-AC02-05CH11231).

References

- [1] A. Trovarelli, P. Fornasiero, Catalysis by Ceria and Related Materials, 2nd ed., Imperial College Press2013.
- [2] R. Ragg, M.N. Tahir, W. Tremel, Solids go bio: Inorganic nanoparticles as enzyme mimics, Eur. J. Inorg. Chem. 2016 (2016) 1906-1915, 10.1002/ejic.201501237.
- [3] W. Liu, M. Flytzani-Shitephanopoulos, Total oxidation of carbon monoxide and methane over transition metal fluorite oxide composite catalysts: I. Catalyst composition and activity, J. Catal. 153 (1995) 304-316, 10.1006/jcat.1995.1132.
- [4] H. Muroyama, H. Asajima, S. Hano, T. Matsui, K. Eguchi, Effect of an additive in a CeO₂-based oxide on catalytic soot combustion, Appl. Catal. A-Gen. 489 (2015) 235-240, 10.1016/j.apcata.2014.10.039.
- [5] I.V. Zagaynov, A.V. Naumkin, Y.V. Grigoriev, Perspective intermediate temperature ceria based catalysts for CO oxidation, Appl. Catal. B-Environ. 236 (2018) 171-175, 10.1016/j.apcatb.2018.05.027.
- [6] G. Spezzati, A.D. Benavidez, A.T. DeLaRiva, Y. Su, J.P. Hofmann, S. Asahina, E.J. Olivier, J.H. Neethling, J.T. Miller, A.K. Datye, E.J.M. Hensen, CO oxidation by Pd supported on CeO₂(100) and CeO₂(111) facets, Appl. Catal. B-Environ. 243 (2019) 36-46, 10.1016/j.apcatb.2018.10.015.
- [7] J. Resasco, L. DeRita, S. Dai, J.P. Chada, M. Xu, X. Yan, J. Finzel, S. Hanukovich, A.S. Hoffman, G.W. Graham, S.R. Bare, X. Pan, P. Christopher, Uniformity is key in defining structure–function relationships for atomically dispersed metal catalysts: The case of Pt/CeO₂, J. Am. Chem. Soc. 142 (2020) 169-184, 10.1021/jacs.9b09156.
- [8] D. Jiang, Y. Yao, T. Li, G. Wan, X.I. Pereira-Hernández, Y. Lu, J. Tian, K. Khivantsev, M.H. Engelhard, C. Sun, C.E. García-Vargas, A.S. Hoffman, S.R. Bare, A.K. Datye, L. Hu, Y. Wang, Tailoring the local environment of platinum in single-atom Pt₁/CeO₂ catalysts for robust low-temperature CO oxidation, Angew. Chem. Int. Ed. 60 (2021) 26054-26062, 10.1002/anie.202108585.
- [9] R. Alcala, A. DeLaRiva, E.J. Peterson, A. Benavidez, C.E. Garcia-Vargas, D. Jiang, X.I. Pereira-Hernández, H.H. Brongersma, R.t. Veen, J. Staněk, J.T. Miller, Y. Wang, A. Datye, Atomically dispersed

- dopants for stabilizing ceria surface area, Appl. Catal. B-Environ. 284 (2021) 119722, 10.1016/j.apcatb.2020.119722.
- [10] E. Aneggi, C. de Leitenburg, G. Dolcetti, A. Trovarelli, Promotional effect of rare earths and transition metals in the combustion of diesel soot over CeO₂ and CeO₂–ZrO₂, Catal. Today 114 (2006) 40-47, 10.1016/j.cattod.2006.02.008.
- [11] H. Muroyama, S. Hano, T. Matsui, K. Eguchi, Catalytic soot combustion over CeO₂-based oxides, Catal. Today 153 (2010) 133-135, 10.1016/j.cattod.2010.02.015.
- [12] J.I. Gutiérrez-Ortiz, B. de Rivas, R. López-Fonseca, J.R. González-Velasco, Catalytic purification of waste gases containing VOC mixtures with Ce/Zr solid solutions, Appl. Catal. B-Environ. 65 (2006) 191-200, 10.1016/j.apcatb.2006.02.001.
- [13] W. Tang, Z. Hu, M. Wang, G.D. Stucky, H. Metiu, E.W. McFarland, Methane complete and partial oxidation catalyzed by Pt-doped CeO₂, J. Catal. 273 (2010) 125-137, 10.1016/j.jcat.2010.05.005.
- [14] T. Tsoncheva, R. Ivanova, J. Henych, M. Dimitrov, M. Kormunda, D. Kovacheva, N. Scotti, V.D. Santo, V. Štengl, Effect of preparation procedure on the formation of nanostructured ceria–zirconia mixed oxide catalysts for ethyl acetate oxidation: Homogeneous precipitation with urea vs template-assisted hydrothermal synthesis, Appl. Catal. A-Gen. 502 (2015) 418-432, 10.1016/j.apcata.2015.05.034.
- [15] Q. Fu, H. Saltsburg, M. Flytzani-Stephanopoulos, Active nonmetallic Au and Pt species on ceria-based water-gas shift catalysts, Science 301 (2003) 935-938, 10.1126/science.1085721.
- [16] R. Si, M. Flytzani-Stephanopoulos, Shape and crystal-plane effects of nanoscale ceria on the activity of Au-CeO₂ catalysts for the water–gas shift reaction, Angew. Chem. Int. Ed. 47 (2008) 2884-2887, 10.1002/anie.200705828.
- [17] M.S. Hegde, G. Madras, K.C. Patil, Noble metal ionic catalysts, Accounts Chem. Res. 42 (2009) 704-712, 10.1021/ar800209s.
- [18] M.D. Krcha, A.D. Mayernick, M.J. Janik, Periodic trends of oxygen vacancy formation and C–H bond activation over transition metal-doped CeO₂(111) surfaces, J. Catal. 293 (2012) 103-115, 10.1016/j.jcat.2012.06.010.

- [19] M. Nolan, Enhanced oxygen vacancy formation in ceria (111) and (110) surfaces doped with divalent cations, J. Mater. Chem. 21 (2011) 9160-9168, 10.1039/C1JM11238D.
- [20] H. Metiu, S. Chrétien, Z. Hu, B. Li, X. Sun, Chemistry of Lewis acid-base pairs on oxide surfaces, J. Phys. Chem. C 116 (2012) 10439-10450, 10.1021/jp301341t.
- [21] K. Kim, J.W. Han, Mechanistic study for enhanced CO oxidation activity on (Mn,Fe) co-doped CeO₂(111), Catal. Today 293-294 (2017) 82-88, 10.1016/j.cattod.2016.11.046.
- [22] D. Tian, K. Li, Y. Wei, X. Zhu, C. Zeng, X. Cheng, Y. Zheng, H. Wang, DFT insights into oxygen vacancy formation and CH₄ activation over CeO₂ surfaces modified by transition metals (Fe, Co and Ni), Phys. Chem. Chem. Phys. 20 (2018) 11912-11929, 10.1039/C7CP08376A.
- [23] C. Riley, S. Zhou, D. Kunwar, A. De La Riva, E. Peterson, R. Payne, L. Gao, S. Lin, H. Guo, A. Datye, Design of effective catalysts for selective alkyne hydrogenation by doping of ceria with a single-atom promotor, J. Am. Chem. Soc. 140 (2018) 12964-12973, 10.1021/jacs.8b07789.
- [24] C. Riley, G. Canning, A. De La Riva, S. Zhou, E. Peterson, A. Boubnov, A. Hoffman, M. Tran, S.R. Bare, S. Lin, H. Guo, A. Datye, Environmentally benign synthesis of a PGM-free catalyst for low temperature CO oxidation, Appl. Catal. B-Environ. 264 (2020) 118547, 10.1016/j.apcatb.2019.118547.
- [25] J.P. Perdew, J.A. Chevary, S.H. Vosko, K.A. Jackson, M.R. Pederson, D.J. Singh, C. Fiolhais, Atoms, molecules, solids, and surfaces: Applications of the generalized gradient approximation for exchange and correlation, Phys. Rev. B 46 (1992) 6671-6687, 10.1103/PhysRevB.46.6671.
- [26] G. Kresse, J. Furthmüller, Efficient iterative schemes for ab initio total-energy calculations using a plane-wave basis set, Phys. Rev. B 54 (1996) 11169-11186, 10.1103/PhysRevB.54.11169.
- [27] G. Kresse, D. Joubert, From ultrasoft pseudopotentials to the projector augmented-wave method, Phys. Rev. B 59 (1999) 1758-1775, 10.1103/PhysRevB.59.1758.
- [28] S.L. Dudarev, G.A. Botton, S.Y. Savrasov, C.J. Humphreys, A.P. Sutton, Electron-energy-loss spectra and the structural stability of nickel oxide: An LSDA+U study, Phys. Rev. B 57 (1998) 1505-1509, 10.1103/PhysRevB.57.1505.

- [29] J. Paier, C. Penschke, J. Sauer, Oxygen defects and surface chemistry of ceria: Quantum chemical studies compared to experiment, Chem. Rev. 113 (2013) 3949-3985, 10.1021/cr3004949.
- [30] D.A. Andersson, S.I. Simak, B. Johansson, I.A. Abrikosov, N.V. Skorodumova, Modeling of CeO₂, Ce₂O₃, and CeO_{2-x} in the LDA+U formalism, Phys. Rev. B 75 (2007) 035109, 10.1103/PhysRevB.75.035109.
- [31] C. Loschen, J. Carrasco, K.M. Neyman, F. Illas, First-principles LDA+U and GGA+U study of cerium oxides: Dependence on the effective U parameter, Phys. Rev. B 75 (2007) 035115, 10.1103/PhysRevB.75.035115.
- [32] J.L.F. Da Silva, M.V. Ganduglia-Pirovano, J. Sauer, V. Bayer, G. Kresse, Hybrid functionals applied to rare-earth oxides: The example of ceria, Phys. Rev. B 75 (2007) 045121, 10.1103/PhysRevB.75.045121.
- [33] M. Huang, S. Fabris, CO adsorption and oxidation on ceria surfaces from DFT+U calculations, J. Phys. Chem. C 112 (2008) 8643-8648, 10.1021/jp709898r.
- [34] M. Capdevila-Cortada, Z. Łodziana, N. López, Performance of DFT+U approaches in the study of catalytic materials, ACS Catal. 6 (2016) 8370-8379, 10.1021/acscatal.6b01907.
- [35] C. Zhao, Y. Xu, Simulated temperature programmed desorption of acetaldehyde on CeO₂(111): Evidence for the role of oxygen vacancy and hydrogen transfer, Top. Catal. 60 (2017) 446-458, 10.1007/s11244-016-0703-y.
- [36] M.V. Ganduglia-Pirovano, J.L.F. Da Silva, J. Sauer, Density-functional calculations of the structure of near-surface oxygen vacancies and electron localization on CeO₂(111), Phys. Rev. Lett. 102 (2009) 026101, 10.1103/PhysRevLett.102.026101.
- [37] H.-Y. Li, H.-F. Wang, X.-Q. Gong, Y.-L. Guo, Y. Guo, G. Lu, P. Hu, Multiple configurations of the two excess 4f electrons on defective CeO₂(111): Origin and implications, Phys. Rev. B 79 (2009) 193401, 10.1103/PhysRevB.79.193401.
- [38] Z. Xu, Y.V. Joshi, S. Raman, J.R. Kitchin, Accurate electronic and chemical properties of 3d transition metal oxides using a calculated linear response U and a DFT + U(V) method, J. Chem. Phys. 142 (2015) 144701, 10.1063/1.4916823.

- [39] M.D. Krcha, M.J. Janik, Challenges in the use of density functional theory to examine catalysis by M-doped ceria surfaces, Int. J. Quantum Chem. 114 (2014) 8-13, 10.1002/qua.24548.
- [40] L. Gerward, J.S. Olsen, Powder diffraction analysis of cerium dioxide at high pressure, Powder Diffr. 8 (1993) 127-129, 10.1017/S0885715600017966.
- [41] G. Henkelman, A. Arnaldsson, H. Jónsson, A fast and robust algorithm for Bader decomposition of charge density, Comp. Mater. Sci. 36 (2006) 354-360, 10.1016/j.commatsci.2005.04.010.
- [42] W. Tang, E. Sanville, G. Henkelman, A grid-based Bader analysis algorithm without lattice bias, J. Phys. Condens. Mat. 21 (2009) 084204, 10.1088/0953-8984/21/8/084204.
- [43] J. Neugebauer, M. Scheffler, Adsorbate-substrate and adsorbate-adsorbate interactions of Na and K adlayers on Al(111), Phys. Rev. B 46 (1992) 16067-16080, 10.1103/PhysRevB.46.16067.
- [44] V. Shapovalov, H. Metiu, Catalysis by doped oxides: CO oxidation by Au_xCe_{1-x}O2, J. Catal. 245 (2007) 205-214, 10.1016/j.jcat.2006.10.009.
- [45] H.A. Hansen, C. Wolverton, Kinetics and thermodynamics of H₂O dissociation on reduced CeO₂(111), J. Phys. Chem. C 118 (2014) 27402-27414, 10.1021/jp508666c.
- [46] G.E. Murgida, M.V. Ganduglia-Pirovano, Evidence for subsurface ordering of oxygen vacancies on the reduced CeO₂(111) surface using density-functional and statistical calculations, Phys. Rev. Lett. 110 (2013) 246101, 10.1103/PhysRevLett.110.246101.
- [47] C. Yang, X. Yu, S. Heißler, P.G. Weidler, A. Nefedov, Y. Wang, C. Wöll, T. Kropp, J. Paier, J. Sauer, O₂ activation on ceria catalysts The importance of substrate crystallographic orientation, Angew. Chem. Int. Ed. 56 (2017) 16399-16404, 10.1002/anie.201709199.
- [48] J.J. Carey, M. Nolan, Dissociative adsorption of methane on the Cu and Zn doped (111) surface of CeO₂, Appl. Catal. B-Environ. 197 (2016) 324-336, 10.1016/j.apcatb.2016.04.004.
- [49] F. Dvořák, M. Farnesi Camellone, A. Tovt, N.-D. Tran, F.R. Negreiros, M. Vorokhta, T. Skála, I. Matolínová, J. Mysliveček, V. Matolín, S. Fabris, Creating single-atom Pt-ceria catalysts by surface step decoration, Nat. Commun. 7 (2016) 10801, 10.1038/ncomms10801.

- [50] P. Bera, K.R. Priolkar, P.R. Sarode, M.S. Hegde, S. Emura, R. Kumashiro, N.P. Lalla, Structural investigation of combustion synthesized Cu/CeO_2 catalysts by EXAFS and other physical techniques: Formation of a $Ce_{1-x}Cu_xO_{2-\delta}$ solid solution, Chemistry of Materials 14 (2002) 3591-3601, 10.1021/cm0201706.
- [51] C.E. García-Vargas, G. Collinge, D. Yun, M.-S. Lee, V. Muravev, Y.-Q. Su, X.I. Pereira-Hernández, D. Jiang, V.-A. Glezakou, E.J.M. Hensen, R. Rousseau, A.K. Datye, Y. Wang, Activation of lattice and adatom oxygen by highly stable ceria-supported Cu single atoms, ACS Catal. 12 (2022) 13649-13662, 10.1021/acscatal.2c04001.
- [52] K. Eguchi, T. Setoguchi, T. Inoue, H. Arai, Electrical properties of ceria-based oxides and their application to solid oxide fuel cells, Solid State Ionics 52 (1992) 165-172, 10.1016/0167-2738(92)90102-U.
- [53] E. Mamontov, T. Egami, Structural defects in a nano-scale powder of CeO₂ studied by pulsed neutron diffraction, J. Phys. Chem. Solids 61 (2000) 1345-1356, 10.1016/S0022-3697(00)00003-2.
- [54] Y.M. Choi, H. Abernathy, H.-T. Chen, M.C. Lin, M. Liu, Characterization of O₂–CeO₂ interactions using in situ raman spectroscopy and first-principle calculations, ChemPhysChem 7 (2006) 1957-1963, 10.1002/cphc.200600190.
- [55] M. Huang, S. Fabris, Role of surface peroxo and superoxo species in the low-temperature oxygen buffering of ceria: Density functional theory calculations, Phys. Rev. B 75 (2007) 081404, 10.1103/PhysRevB.75.081404.
- [56] J.C. Conesa, Surface anion vacancies on ceria: Quantum modelling of mutual interactions and oxygen adsorption, Catal. Today 143 (2009) 315-325, 10.1016/j.cattod.2008.11.005.
- [57] C. Schilling, M.V. Ganduglia-Pirovano, C. Hess, Experimental and theoretical study on the nature of adsorbed oxygen species on shaped ceria nanoparticles, J. Phys. Chem. Lett. 9 (2018) 6593-6598, 10.1021/acs.jpclett.8b02728.

- [58] J. Guzman, S. Carrettin, A. Corma, Spectroscopic evidence for the supply of reactive oxygen during CO oxidation catalyzed by gold supported on nanocrystalline CeO₂, J. Am. Chem. Soc. 127 (2005) 3286-3287, 10.1021/ja043752s.
- [59] Z. Wu, M. Li, J. Howe, H.M. Meyer, III, S.H. Overbury, Probing defect sites on CeO₂ nanocrystals with well-defined surface planes by Raman spectroscopy and O₂ adsorption, Langmuir 26 (2010) 16595-16606, 10.1021/la101723w.
- [60] D. Du, J. Kullgren, K. Hermansson, P. Broqvist, From ceria clusters to nanoparticles: Superoxides and supercharging, J. Phys. Chem. C 123 (2019) 1742-1750, 10.1021/acs.jpcc.8b08977.
- [61] I. Yeriskin, M. Nolan, Doping of ceria surfaces with lanthanum: a DFT + U study, J. Phys. Condens. Mat. 22 (2010) 135004, 10.1088/0953-8984/22/13/135004.
- [62] P.R.L. Keating, D.O. Scanlon, B.J. Morgan, N.M. Galea, G.W. Watson, Analysis of intrinsic defects in CeO₂ using a Koopmans-like GGA+U approach, J. Phys. Chem. C 116 (2012) 2443-2452, 10.1021/jp2080034.
- [63] Z. Wu, Y. Cheng, F. Tao, L. Daemen, G.S. Foo, L. Nguyen, X. Zhang, A. Beste, A.J. Ramirez-Cuesta, Direct neutron spectroscopy observation of cerium hydride species on a cerium oxide catalyst, J. Am. Chem. Soc. 139 (2017) 9721-9727, 10.1021/jacs.7b05492.
- [64] K. Werner, X. Weng, F. Calaza, M. Sterrer, T. Kropp, J. Paier, J. Sauer, M. Wilde, K. Fukutani, S. Shaikhutdinov, H.-J. Freund, Toward an understanding of selective alkyne hydrogenation on ceria: On the impact of O vacancies on H₂ interaction with CeO₂(111), J. Am. Chem. Soc. 139 (2017) 17608-17616, 10.1021/jacs.7b10021.
- [65] M.A. Vannice, An analysis of the Mars–van Krevelen rate expression, Catal. Today 123 (2007) 18-22, 10.1016/j.cattod.2007.02.002.
- [66] M. García-Melchor, N. López, Homolytic products from heterolytic paths in H₂ dissociation on metal oxides: The example of CeO₂, J. Phys. Chem. C 118 (2014) 10921-10926, 10.1021/jp502309r.
- [67] D. Fernández-Torre, J. Carrasco, M.V. Ganduglia-Pirovano, R. Pérez, Hydrogen activation, diffusion, and clustering on CeO₂(111): A DFT+U study, J. Chem. Phys. 141 (2014) 014703, 10.1063/1.4885546.

- [68] J. Xu, J. Harmer, G. Li, T. Chapman, P. Collier, S. Longworth, S.C. Tsang, Size dependent oxygen buffering capacity of ceria nanocrystals, Chem. Commun. 46 (2010) 1887-1889, 10.1039/B923780A.
- [69] T. Désaunay, G. Bonura, V. Chiodo, S. Freni, J.P. Couzinié, J. Bourgon, A. Ringuedé, F. Labat, C. Adamo, M. Cassir, Surface-dependent oxidation of H₂ on CeO₂ surfaces, J. Catal. 297 (2013) 193-201, 10.1016/j.jcat.2012.10.011.
- [70] E.C. Tyo, C. Yin, M. Di Vece, Q. Qian, G. Kwon, S. Lee, B. Lee, J.E. DeBartolo, S. Seifert, R.E. Winans, R. Si, B. Ricks, S. Goergen, M. Rutter, B. Zugic, M. Flytzani-Stephanopoulos, Z.W. Wang, R.E. Palmer, M. Neurock, S. Vajda, Oxidative dehydrogenation of cyclohexane on cobalt oxide (Co₃O₄) nanoparticles: The effect of particle size on activity and selectivity, ACS Catal. 2 (2012) 2409-2423, 10.1021/cs300479a.
- [71] A. Getsoian, V. Shapovalov, A.T. Bell, DFT+U investigation of propene oxidation over bismuth molybdate: Active sites, reaction intermediates, and the role of bismuth, J. Phys. Chem. C 117 (2013) 7123-7137, 10.1021/jp400440p.
- [72] J. Yu, Y. Xu, V.V. Guliants, Propane ammoxidation over Mo–V–Te–Nb–O M1 phase: Density functional theory study of propane oxidative dehydrogenation steps, Catal. Today 238 (2014) 28-34, 10.1016/j.cattod.2014.02.053.
- [73] K. Muthukumar, J. Yu, Y. Xu, V.V. Guliants, Propane ammoxidation over the Mo–V–Te–Nb–O M1 phase: Reactivity of surface cations in hydrogen abstraction steps, Top. Catal. 54 (2011) 605-613, 10.1007/s11244-011-9682-1.
- [74] B. Chen, Y. Ma, L. Ding, L. Xu, Z. Wu, Q. Yuan, W. Huang, Reactivity of hydroxyls and water on a CeO₂(111) thin film surface: The role of oxygen vacancy, J. Phys. Chem. C 117 (2013) 5800-5810, 10.1021/jp312406f.
- [75] M. Nolan, G.W. Watson, The surface dependence of CO adsorption on ceria, J. Phys. Chem. B 110 (2006) 16600-16606, 10.1021/jp062499a.
- [76] G.N. Vayssilov, M. Mihaylov, P.S. Petkov, K.I. Hadjiivanov, K.M. Neyman, Reassignment of the vibrational spectra of carbonates, formates, and related surface species on ceria: A combined density

functional and infrared spectroscopy investigation, J. Phys. Chem. C 115 (2011) 23435-23454, 10.1021/jp208050a.

[77] C. Yang, L.-L. Yin, F. Bebensee, M. Buchholz, H. Sezen, S. Heissler, J. Chen, A. Nefedov, H. Idriss, X.-Q. Gong, C. Wöll, Chemical activity of oxygen vacancies on ceria: A combined experimental and theoretical study on CeO₂(111), Phys. Chem. Chem. Phys. 16 (2014) 24165-24168, 10.1039/C4CP02372B. [78] C. Zhao, C. Watt, P.R. Kent, S.H. Overbury, D.R. Mullins, F.C. Calaza, A. Savara, Y. Xu, Coupling of acetaldehyde to crotonaldehyde on CeO_{2-x}(111): Bifunctional mechanism and role of oxygen vacancies, J. Phys. Chem. C 123 (2019) 8273-8286, 10.1021/acs.jpcc.8b08535.

[79] S. Bhasker-Ranganath, M.S. Rahman, C. Zhao, F. Calaza, Z. Wu, Y. Xu, Elucidating the mechanism of ambient-temperature aldol condensation of acetaldehyde on ceria, ACS Catal. 11 (2021) 8621-8634, 10.1021/acscatal.1c01216.